Segmentation, Analysis, and Modelling of Microstructure in Cortical Bone based on X-ray Microtomography

Elin Törnquist

May 2017

Master's Thesis in Biomedical Engineering

Faculty of Engineering, LTH

Department of Biomedical Engineering

Supervisors: Anna Gustafsson
              Ass. Prof. Hanna Isaksson
Examiner: Ass. Prof. Ingrid Svensson

Abstract

The microstructure in cortical bone greatly affect the toughness of the bone and the crack propagation during fracture. The two main structural features, Haversian canals and osteons, have been previously studied in order to increase the knowledge of the biomechanics of bone. In studies where X-ray microtomography has been the imaging method of choice, the microstructure has been analysed based on manual segmentation, a method which is difficult and tedious on larger sample volumes.

X-ray microtomograms, or μCT images, are gray scale 2D images, which can be rendered into a 3D volume, where the pixel intensity corresponds to the absorption coefficient of the material in the object. Material that absorbs a lot of X-ray radiation will show up as high intensity pixel whilst material that absorbs little will show up as low intensity pixel, just as in a normal radiogram. μCT is best used on samples containing structures with varying absorbtion properties as this will enable good contrast between the structures.

In this project, a semi-automatic method for segmenting the microstructures Haversian canals and osteons in μCT images of cortical bovine bone was implemented. Based on this segmentation, a simplified model was built for future Finite Element Modelling. K-means clustering with nine clusters was chosen as segmentation method. By identifying which clusters correspond to what pixel intensities, and hence to what tissue type, it was possible to segment out Haversian canals, and osteons in the μCT images. The simplified model was based on principal component analysis of the segmented canals in 3D, and circle fitting on Haversian canals, and osteons in 2D.

The generated segmentations provided enhanced visibility of the microstructure. Based on porosity, and volume analysis, the segmentation pipeline gave good results for the Haversian canals, but was less accurate in differentiating between osteonal tissue and tissue with similar absorption properties embedded in the interstitial bone. Porosity measurements on the segmentations corresponded with previous studies. The radii of the osteons and the Haversian canals, generated by the simplified model, agreed well with previous studies, and the method overcame the issue with unclear osteonal boundaries by using the segmentation of the Haversian canals as a base.

1 Preface

This Master's Thesis was carried out during the fall of 2016 and spring of 2017, at the Department of Biomedical Engineering, in collaboration with the Division of Solid Mechanics, both at Lund University.

2 Acknowledgments

I would like to thank my supervisors, Anna Gustafsson and Hanna Isaksson, for guiding and assisting me during this project, and also for giving me the opportunity to participate in some activities outside the scope of this project. I would also like to thank Stephen Hall, and the 4D Imaging Lab at the Department of Solid Mechanics, LTH, for the acquisition of the μCT images that are the basis of this project. Lastly, thank you to all the wonderful people in the Biomechanics group, you have made my time spent on this project not only educative but also enjoyable and fun.

Contents

3   Introduction

Bone is a complex tissue with important properties for the biomechanics of an organism. The correlation between structure, at different hierarchical levels, and mechanical properties is not yet completely known and continues to be a field for active research.

Cortical bone has a very complex hierarchical structure that greatly affects the stiffness, and toughness of the bone. Crack propagation is affected by all structures at different length scales; in this project the microstructure of cortical bone, i.e. more than one osteon, is the length scale of interest. Earlier studies have looked at radial 2D models of cortical bone, either by randomly generating the geometry based on statistical analysis of actual samples [Li et al., 2013], or by fitting ellipses to hand segmented structures in microscopy images [Mischinski and Ural, 2011]. [Demirtas et al., 2016] used a 3D model based on extruded transverse microscopy images in which the microstructures had been approximated by ellipses after hand segmentation, as in [Mischinski and Ural, 2011]. Studies using 2D models in the longitudinal plane were not found, neither were any studies where the microstructure was directly modelled based on segmentations of microstructures in a sample.

Visualization of microstructure using manual segmentation, where structures are outlined by hand, is tedious and impractical on larger samples. In this project a semi-automatic method for segmentation of cortical microstructure is implemented. Based on the segmentation a simplified model is created for future implementation of Finite Element models aimed to validating experimental data collected during mechanical testing of cortical bovine bone.

Within a larger multiscale mechanics project, aimed to researching the fracture mechanics of cortical bone at different hierarchical levels, a number of samples of cortical bovine bone were tested in tension and analysed using Digital Image Correlation (DIC), Small Angle X-ray Scattering (SAXS), and Wide Angle X-ray Scattering (WAXS). The experimental setup is shown in Fig. 1. Using DIC surface strains were analysed based on recording a randomized speckle pattern on the surface of the sample at different time points during the experiment, and correlating the scatter pattern at these time points. By analysing SAXS and WAXS data, information about the orientation and deformation of collagen and min-

eral in the sample was gathered. In order to correlate the results from the tensile test to the microstructure in the samples, the samples were imaged using X-ray Microtomography, resulting in the gray scale images that are segmented and analysed in this Master's Thesis project.
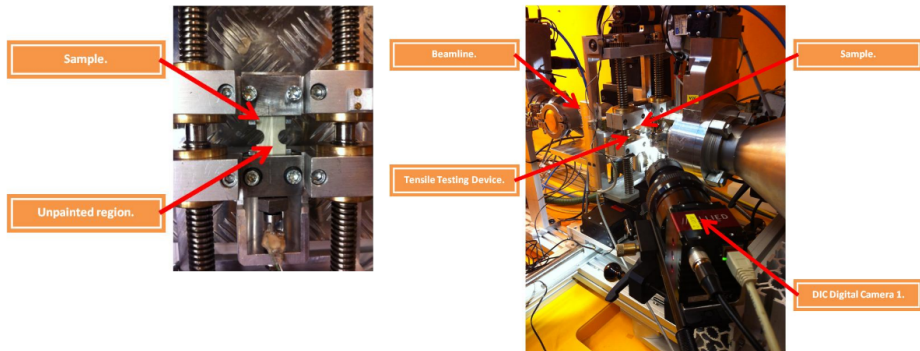
Figure 1: Experimental setup for the tensile testing of the bone samples [Mathavan]. The experiments were carried out by PhD student Neashan Mathavan at the I911-4 beamline at MAXLAB. [Courtesy of Mathavan].

4   Aims and Objective

The aim of this Master's Thesis project was to develop a semi-automatic method for segmentation of X-ray microtomography (μCT) images of cortical bone in order to separate the microstructures *Haversian canals*, and *osteons* which play an important role in the mechanics of crack propagation. The resulting segmentation needs to represent the real structures in terms of geometry, volume, and porosity. Based on the segmentation, a simplified model that could be used to model crack propagation in a Finite Element (FE) software was to be developed. The model should be representative of the structures in terms of radii, placement, and tilt, but be simple enough for easy implementation and simulation in the FE software.

5 Background and Theory

5.1 Bone

At macro level bone is made up of trabecular (spongy), and cortical (compact) bone [Martini, 2012]. Fig. 2 depicts a human femur where, as with all long bones and most other bone types, the distal and proximal epiphyses contain trabecular bone. The shaft and outer layers of the epiphyses are made up of cortical bone. Trabecular bone is found in regions of the bone where the stresses during loading are multidirectional, whilst cortical bone is found in regions where stresses are mainly unidirectional.
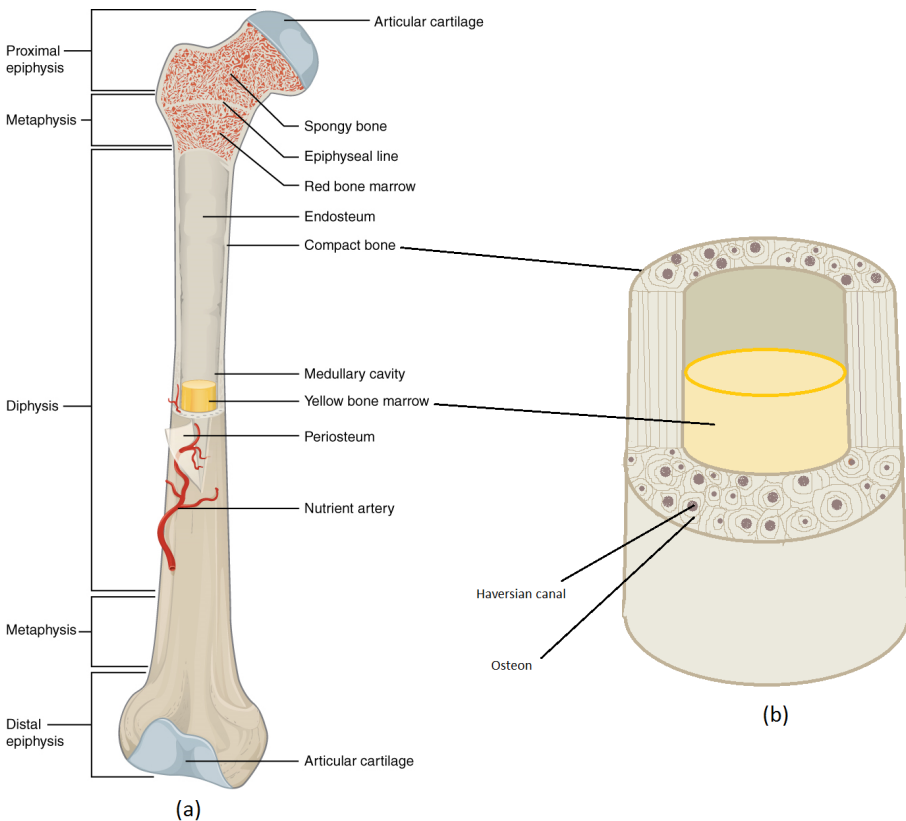

Figure 2: Anatomy of a long bone. (a) Overview. (b) Cortical (compact) bone. [Adapted after OpenStax College, 2013].

5.1.1 The Microstructure of Cortical Bone

Cortical bone has a complex hierarchical structure (see Fig. 3). At sub-nano scale the structure is made up of collagen molecules interwoven by mineral crystals [Robling and Stout, 2008]. These structures form collagen fibrils, which in turn form collagen fibres at nano-scale. At sub-micro scale the collagen fibres form lamellae surrounding so called *Haversian canals*. The lamellar structure is known as *osteons* and have a lower mineral content than the surrounding bone matrix, or *interstitial bone*. However, the mineral density varies highly between osteons depending on their age [Budyn et al., 2010, 2012]. The Haversian canals are hollow canals that permeate the bone, enclosing blood vessels and nerve fibres. They are interconnected by branching canals called *Volkmann's canals* which also enclose blood vessels and nerve fibres but lack the surrounding osteonal structure [Maggiano et al., 2016].
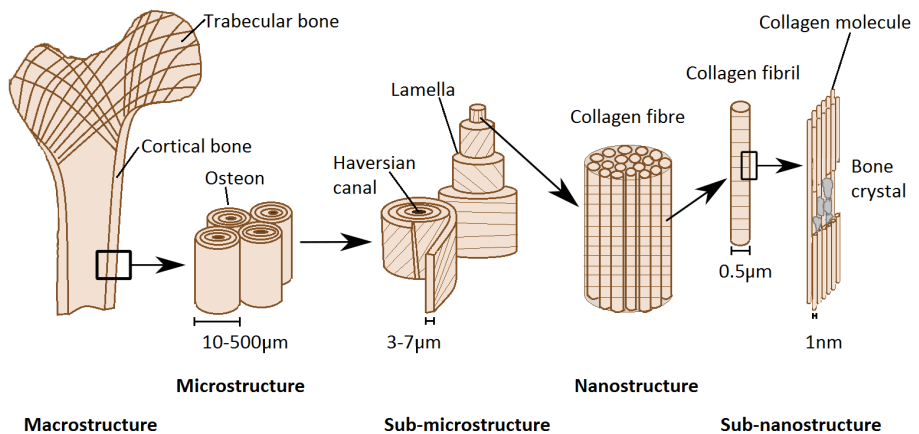
Figure 3: Hierarchical structure of cortical bone seen at different size scales. [Redrawn from Ritchie, 2010]

Bone is a dynamic tissue, i.e. the structure and components change over time due to growth, modelling and remodelling [Robling and Stout, 2008; Budyn et al., 2010, 2012; Maggiano et al., 2016; Ritchie, 2010]. Growth is regulated by the genetic setup of the individual organism, and sees to increase in length and thickness (diameter) of the bone. Modelling modifies the genetic base structure by optimizing the structure for mechanical loading experienced by the individual; the architecture and mass

of the bone is altered as bone is added (*formation*) or removed (*resorption*) from surfaces that experience more or less mechanical loading. The result of growth and modelling in normal bone is an organized structure made up of parallel sheets of primary lamellar bone, called *primary osteons*, permeated by canals, as well as by *primary vascular channels*, or *non-Haversian canals*. Non-Haversian canals are channels containing vasculature as, during modelling, some periosteal blood vessels become incorporated into the cortical lamellar matrix. Some, but not all, such primary vascular channels have a few concentric lamellae deposited around them creating a primary osteon around the non-Haversian canal. The number of non-Haversian canals decrease with age and can hence be used to determine the age of the tissue.

Growth and normal modelling stops when the skeleton reaches maturity. Remodelling differs from modelling in that both resorption and formation occurs at the same location of the bone. The remodelling sequence, *activation→resorption→formation*, removes and replaces bone structural units (BMUs, see Fig. 4), which are complex arrangements of cells that cut through interstitial cortical bone in mainly longitudinal direction. The resulting structures - canals and surrounding hypomineralized bone - are denoted *secondary osteons* of which there are many subtypes. The leading region of the BMU is called the *cutting cone* and is lined with *osteoclasts* which are cells specialized in resorbing bone. Directly after the cutting cone and its osteoclasts is a small region called the *resorptive bay* lined with *mononuclear cells* whose exact function is unclear.Following the resorptive bay is the *closing cone* which is lined with *osteoblasts*, a cell type specialized in the formation of bone. Osteoblasts deposit layers of osteoid (unmineralized bone matrix) which leads to a centripetally layered structure of osteonal lamellae once it is mineralized. Once the deposition of osteoid ceases, the Haversian canal is left in the center of the osteon. Some osteoblasts get trapped in the osteoid and differentiate into *osteocytes* which are the most abundant type of bone cell [Langer and Peyrin, 2016]. Osteocytes communicate with each other through dendritic precesses which, upon the apoptosis of the osteocyte, leave a network of small canals called *canaliculi*. The canaliculi connect the hollow spaces left by the osteocytes, called *lacunae*, making up what is called the *lacuno-canalicular* network (LCN).
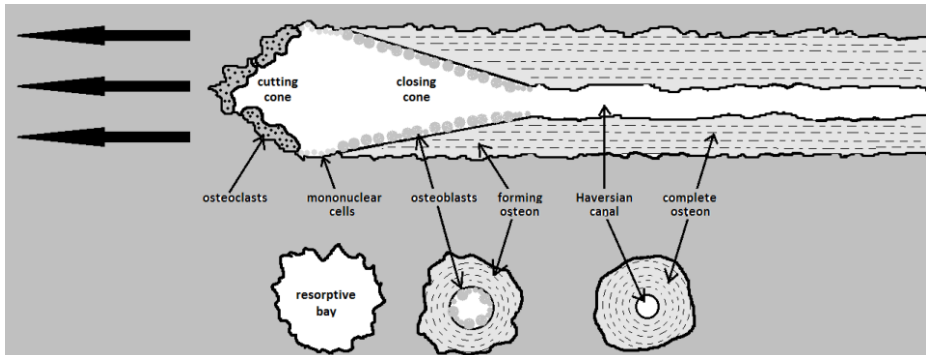
Figure 4: (**top**) Longitudinal view of a BMU moving through bone from right to left. (**bottom**) Schematic illustrations of an evolving osteon and Haversian canal, corresponding to selected transverse sections of the BMU system. [Redrawn after Robling and Stout, 2008]

Secondary osteons in human cortical bone are generally 200-300μm in diameter, with the enclosed Haversian canal at 50-90μm in diameter [Maggiano et al., 2016; Ritchie, 2010; Ritchie et al., 2005]. In cortical bovine bone the dimensions are smaller; osteons have an average diameter of around 150-200μm, and Haversian canals have an average diameter of around 30-50μm (see Tab. 1), depending on the age of the animal.

Table 1: Diameters of microstructure in cortical bovine bone, according to different studies.

Study	Haversian canal (μm)	Osteon (μm)
Budyn et al., 2010,2012	37	179
Zhang et al., 2014	30	192.7
Carnelli et al., 2013	50	200

5.1.2   Crack Propagation and Microstructure

The formation and propagation of micro cracks is heavily affected by the size and density of the osteons, the porosity of the cortical tissue, as well as by the orientation of the osteons [Mischinski and Ural, 2011; Budyn et al., 2010, 2012; Ritchie et al., 2005; Koester et al., 2008]. It is much easier to split bone in the longitudinal direction, parallel with the main osteonal orientation, than it is in the transverse direction, perpendicular to the osteons. As is described in section 5.1.1 The Microstructure of Cortical Bone the osteon is created at a later time point than the interstitial bone

and is hence less mineralized, resulting in a lower mechanical stiffness and toughness [Budyn et al., 2010]. The longitudinal orientation of the osteons is what constituted the anisotropic properties of the bone, resulting in different mechanical properties depending on the orientation.

5.2 X-ray Microtomography

X-rays are commonly used for medical imaging of internal structures in the body. The basic principle is to radiate the object of interest, with some dose X_i, and measure the amount of radiation that has permeated the object, X_e. This gives a measurement of how much the incident X-ray photons have interacted with the material in the object, $\mathsf{X}_a = \mathsf{X}_e - \mathsf{X}_i$. X-ray photons interact with the electrons in the material, which means that depending on the size of the atoms in the material, and hence the binding energies of the atomic electrons, different atoms will interact with different photon energies.

Medical X-ray imaging uses photon energies of 15-150 keV [Bushberg et al., 2012]. Depending on the energy of the photons, and the mass of the atoms with which the photons interacts, four different types of interactions (scattering or absorption) with atoms will dominate the attenuation of the X-rays: Rayleigh scattering, Compton scattering, photoelectric absorption, and pair production. Only Rayleigh scattering, Compton scattering, and the photoelec-

Figure 5: The energy dependence of the Mass Attenuation Coefficient of cortical bone [Courtesy of Commons, 2001].

tric effect play a role for diagnostic radiology, as pair production requires energies higher than those used. The energy dependence of the Mass Attenuation Coefficient (a type of absorption cross section per unit mass) of cortical bone is seen in Fig. 5. From the graph it is evident that the most prominent attenuation process is the photoelectric effect.
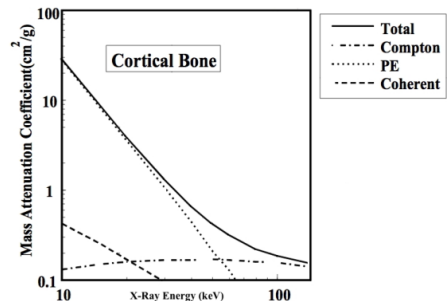
The conventional X-ray set up creates two dimensional images which are a superimposition of interactions with all structures inside the object [Hsieh, 2009] (illustrated in Fig. 6). This means that it is not possible

13

to know where, depth wise, a structure is located inside the object being X-rayed.
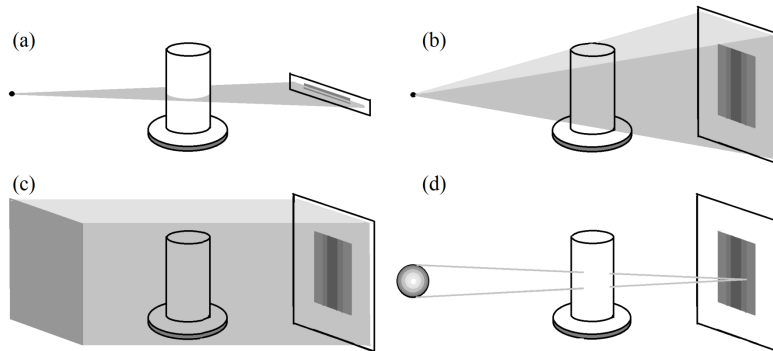
Figure 6: Illustrative sketch of different plane X-ray acquisition configurations. (a) In a fan beam the projections are acquired in slices. (b) A cone beam, and (c) a parallel beam, enable acquiring a full 2D projection in a single step. (d) Illustration of the affect of a non-point source, where the intensity registered by the detector at a specific point consists of many different rays from a larger volume of the object. [Redrawn after Landis and Keane, 2010].

Computerized Axial Tomography (CT or CAT) scans solves the depth resolution issue by acquiring a series of 2D radiographs whilst the imaged object is rotated around a single axis, or whilst the source and detector are rotated around the object [Landis and Keane, 2010]. These 2D images are then used to construct a 3D image of the object. Each horizontal pixel strip in a 2D image is Fourier-transformed, filtered, and then inverse-Fourier-transformed before the tomogram is obtained using back-projection calculations [Mizutani and Suzuki, 2012] (see Fig. 7).

Figure 7: Principle of tomographic reconstruction, courtesy of [Redrawn after Mizutani and Suzuki, 2012]. (A) 2D images are acquired by rotation the object. (B) Each horizontal pixel strip in the 2D image is subjected to Fourier transformation, filtering, and inverse Fourier transformation. (C) Back-propagation is used to obtain the tomogram.
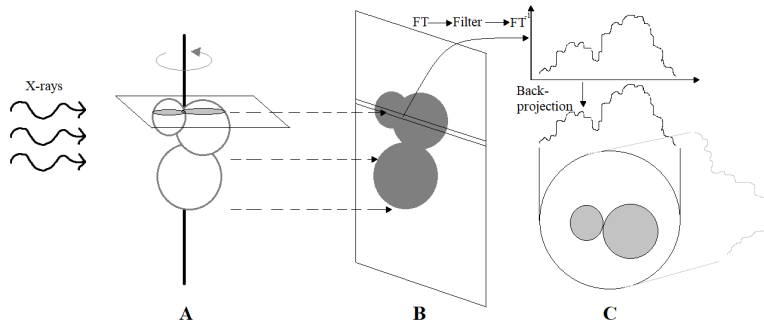
A number of factors contribute to the quality of a tomogram and the reduction of artefacts [Boas and Fleischmann, 2012]. The resolution of the detector needs to be high enough to be able to resolve the structures of interest, and as little scattering and motion as possible needs to occur. Completely monochromatic X-rays, with high brilliance, is also desirable in order to get a high photon count, and low pixel intensity dependence on photon energy.

If the detector is defected or miscalibrated the tomogram will present with ring artefacts, i.e. bright or dark rings centred around the center of rotation; the fix is to re-calibrate or change the detector [Boas and Fleischmann, 2012].

X-ray tomogram noise is in the form of Poisson noise, which occurs due to the statistical error when the photon count is low, and shows as random thin bright or dark streaks mainly in the direction of greatest attenuation [Boas and Fleischmann, 2012]. By increasing the brilliance the noise is reduced, but at the same time the resolution is decreased since the differences in attenuation between regions in the object being scanned are less influential. Iterative reconstruction algorithms have been implemented to reduce the issue with noise in high resolution tomograms. *Model-based iterative reconstruction* (MBIR) is one such method that decouples the noise and image quality, and hence allows for high resolution tomograms with low noise, at lower X-ray brilliance.

For polychromatic X-ray sources, beam hardening causes artefacts in form

of dark streaks between regions with high attenuation, or along the long axis of a region with high attenuation [Boas and Fleischmann, 2012]. The low energy photons in the polychromatic X-rays are more easily attenuated than the higher energy photons leading to a beam transmission that diverges from that of a monochromatic beam where all of the photons that hit the detector have interacted with the atoms in the object in the same way due to their coherent energy. Low energy X-rays are attenuated primarily due to the photoelectric effect, which means the attenuation is proportional to Z^3/E^3 (Z is the atomic number, and E is the energy of the photons), whilst high energy photons are attenuated primarily due to Compton scattering, which means the attenuation is proportional to $1/E$. For high atomic number materials, such as bone, this means that the attenuation differs for different energy photons and hence the resulting absorption profile will not only convey the attenuation in the object but will also be a function of the photon energies. A common fix for beam hardening is to correct for it by assuming an average amount of beam hardening based on the measured attenuation. Higher atomic number materials will need an iterative process, based on forward projecting information about the distribution of high attenuation regions, in order to correct for the beam hardening as it is higher than average.

Compton scattering causes photons to end up in different detector pixels due to them changing directions instead of transferring all of their energy to the atoms in the object being imaged [Boas and Fleischmann, 2012]. Reducing scatter is done by employing anti-scatter grids in front of the detector, or by subtracting an estimate of the scatter from the measured attenuation.

Both scattering and beam hardening causes dark streaks along the lines of greatest attenuation for highly attenuated X-ray beams, since more photons than expected are being detected at these sites [Boas and Fleischmann, 2012]. Scanning at higher energies reduces the beam hardening but also the contrast between regions with different attenuation properties.

X-ray Microtomography, or micro CT (μCT), is a method of visualizing structures at micro scale using X-rays. Both the characteristics of the detector and the geometry of the X-ray beam affect the spatial resolution in the acquired image. The pixel size of the detector must be less than or equal to the size of the objects one wants to visualize; one megapixel detectors (e.g. 1024 by 1024) are commonly used. The spot size of a point

source (fan or cone beam) affects the resolution in the same way, as is illustrated in Fig. 6b. The smaller the spot size the better as the photons hitting a particular pixel on the detector can be traced back through the object with more precision, resulting in a better reconstruction of the positions of structures in the object, and less noise in the final image. In reality, optics are necessary in order to get a small enough point source. Since X-rays refract very weakly in most practical materials, diffractive optics (Fresnel zone plates) can be used to focus the beam [Langer and Peyrin, 2016]. For the optics to work properly the X-ray source must be monochromatic which puts restrictions on the source used[1]. The source must also have parallel characteristics and have a high brilliance in order to obtain high spatial resolution [Mizutani and Suzuki, 2012]. For N-dimensional images ($N > 2$) the spatial sampling should be less than $1/2\sqrt{N}$ times the spatial resolution, i.e. the width of a pixel should be less than $1/2\sqrt{N}$ times the spatial resolution, since the Nyquist criterion[2] is not enough for visualizing 3D structures using X-ray microtomography.

5.3   Segmentation

Image segmentation aims at partitioning an image into regions with similar properties, and is a problem being actively researched [Bishop, 2009; Szeliski, 2011]. Depending on the type of image one wants to segment different methods have been developed, three of which will be briefly mentioned here.

Thresholding is applicable to gray scale images, and uses pixel intensity intervals as partitions. Pixels bellow a certain value are set to zero (black) and pixels above the value are set to one (white), resulting in a binary image.

Colour-based methods can be applied to both gray scale and colour images, and uses the different colours present in the image as partition. A pixel in a colour image has a colour based on a combination of base colours,

---

[1]Synchrotron radiation sources usually monochromizes their X-rays in order to a specific X-ray energy but most laboratory micrographs are equipped with micro-focus X-ray generators which do not use a monochromator [Mizutani and Suzuki, 2012]. Hence, X-rays from laboratory generators can not always be used together with the optics necessary for microtomography.

[2]The sampling frequency must be at least twice as high as the highest frequency of interest in order to be able to avoid aliasing [Hägglund, 2012].

17

and hence pixels with primarily base colour X can be distinguished from pixels with base colours Y, and Z.

Active contours are methods that detect boundaries between objects in images, and iteratively moves to find the best solution [Szeliski, 2011]. The methods can be used on any image type where the contrast between different objects in the image is high enough.

5.3.1 Segmentation Using K-means Clustering

K-means clustering is a method used for partitioning multidimensional data points, $\{\mathbf{x}_1, ..., \mathbf{x}_N\}$, into K clusters [Bishop, 2009]. Applied to image segmentation it is a type of colour-based method since the resulting segmentation can have more clusters than two, compared to thresholding where the segmentation results in a binary image. The gray scale images acquired by X-ray tomography are well suited for this type of segmentation method as the information given by the images (pixel intensity) is directly related to the properties of the structures in the object that was imaged. In the case of cortical bone, the pixel intensities are directly related to the type of microstructure being imaged: haversian canals being represented by low intensity pixels, and osteons by middle intensity pixels. Clustering pixels based on intensity hence results in a segmentation of the microstructures.

The clustering is done based on the distances between the points $\mathbf{x}_n$ and the center of the clusters. Assuming the data points being D-dimensional, a set of D-dimensional vectors μ_k, where $k = 1, ..., K$, are introduced and can be considered to represent the centres of the K clusters into which the data points are to be partitioned. The partitioning becomes an optimization problem in which the goal is to find a set of vectors, $\{\mu_k\}$, and an assignment of data points to clusters that minimize the sum of the squares of the distances of each data point $\mathbf{x}_k$ to its closest vector μ_k. The objective function is

$$ J = \sum_{n=1}^{N} \sum_{k=1}^{K} r_{nk} \|\mathbf{x}_n - \mu_k\|^2 \tag{1} $$

where $r_{nk} \in \{0, 1\}$ is a set of binary indicator variables that correspond to each data point $\mathbf{x}_n$. r_{nk} describe which cluster k the data point $\mathbf{x}_n$ is

assigned to so that $r_{ni} = 1$ if $\mathbf{x}_n$ is assigned to cluster i and $r_{nj} = 0$ if $j \neq i$. This is known as the 1-of-K coding scheme. To find which values of r_{nk} and μ_k that minimize J an iterative process is used in which, at each iteration, two successive steps are performed, corresponding to successive optimization of the sought after values. In the first step some initial values are chosen for μ_k, and J is minimized with respect to r_{nk} whilst keeping μ_k fixed. In the second step J is minimized with respect to μ_k whilst keeping r_{nk} fixed. This two-step optimization is then repeated until convergence, i.e. no data points are re-assigned to new clusters, or until some maximum number of iterations is reached. The initial values chosen for μ_k can be chosen randomly or as a subset of the data points $\mathbf{x}_n$; if they are chosen randomly a larger number of iterations will usually be needed in order to reach convergence. Determining r_{nk} in the first iteration is done by assigning the nth data point to its closest cluster center, as per

$$
r_{nk} = \begin{cases} 1 & \text{if } k = \arg \min_j \|x_n - \mu_j\|^2 \\ 0 & \text{otherwise.} \end{cases} \tag{2}
$$

This is possible since J is a linear function of r_{nk} and the terms involving different n are independent which means that the optimization for each n can be done separately by choosing r_{nk} to be 1 for which ever cluster k that minimizes $\|x_n - \mu_k\|^2$. Since J is a quadratic function of μ_k the second step in the optimization process is done by setting the derivative of J with respect to μ_k to zero and solving for μ_k, as per

$$
\frac{\delta J}{\delta \mu_k} = -2 \sum_{n=1}^{N} r_{nk}(\mathbf{x}_n - \mu_k) = 0 \tag{3}
$$

$$
\rightarrow \mu_k = \frac{\sum_n r_{nk}\mathbf{x}_n}{\sum_n r_{nk}} \tag{4}
$$

The name *K-means clustering* comes from Eq. 4 which, in words, say that "μ_k is equal to the *mean* of all data points $\mathbf{x}_n$ assigned to cluster k". Since each iteration of the algorithm reduces the value of the objective function the method is sure to converge, however there is a risk of convergence to a local minimum instead of a global minimum which leads to an incorrect partitioning of the data points. This can be dealt with by repeating the

clustering M times, choosing different initial guesses of μ_k, and selecting the best optimization, i.e. the lowest value of the minimized objective function. Another issue with the algorithm is its slowness as in each iteration the Euclidean distance in Eq. 1 must be computed.

A variant is the K-means++ algorithm, where a center, c_1, is chosen heuristically by selecting some data point uniformly at random. It then computes the distances between the center and each other data point, $\mathbf{x}_i$; the distance between center j and data point i is denoted $d(x_i, c_j)$. The next center, c_2 is selected at random from the data points with probability

$$\frac{d^2(x_i, c_1)}{\sum_{i=1}^{N} d^2(x_i, c_1)}, \quad N = 1, ..., n \tag{5}$$

Choosing center j is hence done by computing the distances from each data point to each center, and assigning each data point to its closest center. Each subsequent center is then chosen with a probability proportional to the distance from itself to the closest already chosen center until K centres have been chosen. It has been shown by [Lloyd, 1982] that this algorithm, compared to the standard K-means, converges faster.

6 Method

6.1 Samples

Samples of cortical bovine bone, taken from different locations on the femoral shaft (see Fig. 2), have been used in this project. Sample IDs, and corresponding location in the femur are found in Tab. 2, where L denotes samples cut longitudinally to the long axis of the bone, and T denotes samples cut transversal to the bone surface (see Fig. 8). The different cuts were employed in order to obtain samples with microstructure in different orientations relative to the cut, which in turn would enable me-

Figure 8: Description of the difference between samples labelled L (longitudinal), and T (transverse). Longitudinal samples were cut out parallel to the longitudinal orientation of the collagen fibres, and osteons in the diaphysis of the femur. Transverse samples were cut out tangential to the bone surface. Adopted from [Martini, 2012].

chanical testing in two different orientations relative to the microstructural orientation. Tab. 2 shows the IDs given to the samples. Samples denoted S were to be imaged using SAXS during tensile testing and image stacks denoted W were to be imaged using WAXS during tensile testing. Samples with the same IDs in respect to cut and numbering were taken as a series from the same location in the femur, in order for similar microstructure to be analysed through both DIC/SAXS, and DIC/WAXS[3].
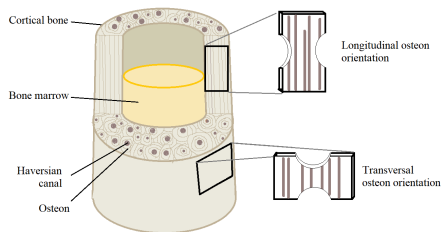
---

[3]The experimental setup did not make simultaneous SAXS and WAXS measurements possible.

Table 2: Sample ID, and location in femur. Samples with common IDs were taken from the same site, as consecutive slices. Physical size and thickness for all samples is found in Appendix A.1.)

ID	Location	Tensile test	SAXS	WAXS
P1	-	Yes	-	-
P2	-	Yes	-	-
1L	Distal diaphysis	No	-	-
1LW	Distal diaphysis	No	No	Yes
1LW Extra	Distal diaphysis	No	No	Yes
2LW	Proximal diaphysis	No	No	Yes
2LS	Proximal diaphysis	No	Yes	No
2LS Extra	Proximal diaphysis	No	Yes	No
3L	Proximal diaphysis	Yes	No	Yes
3LW	Proximal diaphysis	No	No	Yes
3LW Extra	Proximal diaphysis	No	No	Yes
3LS	Proximal diaphysis	No	Yes	No
4L	Proximal diaphysis	No	-	-
4LW	Proximal diaphysis	No	No	Yes
4LS	Proximal diaphysis	Yes	Yes	No
5L	Mid-diaphysis	No	-	-
5LS	Mid-diaphysis	No	Yes	No
1TW	Mid-diaphysis	No	No	Yes
1TS	Mid-diaphysis	Yes	Yes	No
2TS	Mid-diaphysis	Yes	Yes	No
4TW	Mid-diaphysis	No	No	Yes
4TW Extra	Mid-diaphysis	No	No	Yes
4TS	Mid-diaphysis	Yes	Yes	No
5TS	Mid-diaphysis	Yes	Yes	No
6T	Mid-diaphysis	No	-	-
6TW	Mid-diaphysis	No	No	Yes
6TS	Mid-diaphysis	No	Yes	No

All samples were imaged using a 3D X-ray microscope (Zeiss Xradia XRM 520) located at the 4D Imaging Lab at LTH [Solid Mechanics]. In addition, two samples from a pilot experiment, where tensile test were conducted, were imaged and used; these samples were given IDs P1 and P2 (P denotes their involvement in the *pilot* experiment). The samples were wrapped in wet gauze, in order to retain moisture, and stacked in groups

of five. Each group was put into a plastic tube to be mounted, with coronal surfaces facing the X-ray source, at a distance of 62 mm from the source, which was at a voltage of 80 kV, and 38 mm from the detector. The exposure time was set to 5 seconds and 2501 projections were obtained, yielding a homogeneous voxel[4] size of 9.25 μm with a binning of one pixel. The slice thickness of 9.25μm rendered 1,647-2,012 images per sample, depending on the physical thickness of the sample. As the samples were imaged in groups of five each sample had to be manually isolated before further analysis could be done. The slices corresponding to one and the same sample were stacked together to create one image file per sample (see Fig. 9).
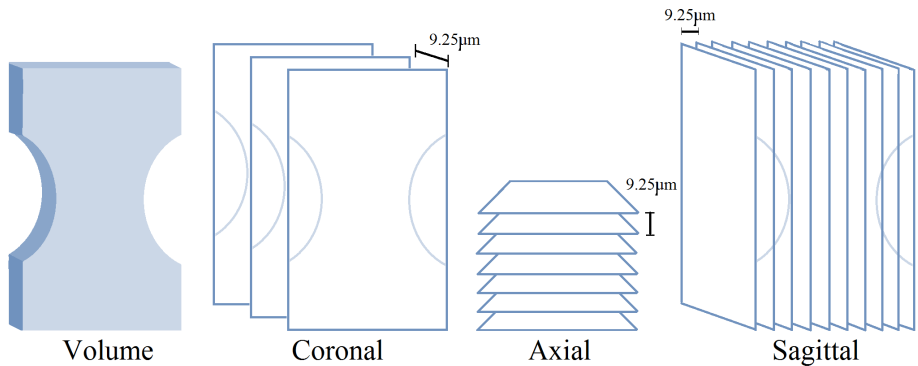

Figure 9: Principle sketch of the stacking of images corresponding to a sample volume. The isotropic voxel size enables easy re-slicing in any orientation.

Ten of the samples (Tab. 2) were imaged before the start of this Master's Thesis project (see Fig. 10). Six of the samples (3L, 4LS, P1, P2, 1TS, and 4TS) had been used in tensile testing which caused them to present with cracks. The remaining samples (see Fig. 11) were imaged during the duration of this project, with slightly differing settings, resulting in images with somewhat different voxel sizes (9.250-9.252μm) and with different pixel intensities. Three samples (4LW, 6T, and 6TW) were imaged at both occasions.

The bone samples varied somewhat in size as the resulting image stacks from the micro CT imaging varied in number of images. In order to analyse porosity and microstructure thickness a manageable sample size, with a representative microstructure that was clearly visible, was chosen

---

[4]Volume element, or 3D pixel.

in the form of two sub-stacks from different locations in the notches in the sample stack. All sub-stacks were of approximately the same volume $(2.927 \pm 0.001 \text{ mm}^3)$[5] so that they would be comparable, and be equally representable for their sample. For all sub-stacks 148 slices were chosen, making the sub-sample depth $1.369\mu\text{m}$. As the samples had slightly different thickness no uniform height and width could be chosen for all sub-stacks.

Fig. 11 show coronal views of the samples from the second imaging round. Fig. 10i, and Fig. 11r, as well as Fig. 10j, and Fig. 11t show the same sample but from different acquisition events.

---

[5]The volume chosen was inspired by the sample volumes used by [Demirtas et al., 2016] (1.0413mm^3) and [Koester et al., 2008] (12.3mm^3).

(a) P1 **(b)** P2 **(c)** 1LW **(d)** 3L

(e) 4LW **(f)** 4LS **(g)** 1TS **(h)** 4TS
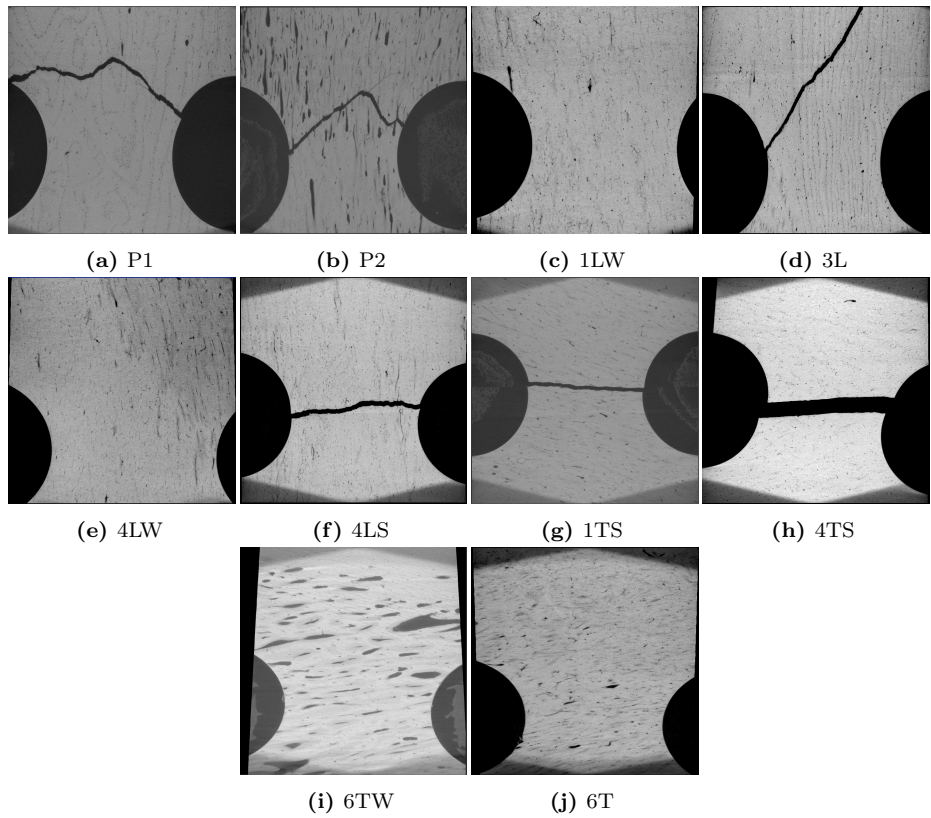
(i) 6TW **(j)** 6T

Figure 10: Coronal views of raw images from mid-slices of the ten samples imaged during the first acquisition, each denoted by its ID. The differences in position is due to how the samples were stacked together in groups of five during the acquisition of the images. Samples 4LS, 1TS, 4TS, 6TW, and 6T display beam hardening (the darker areas at the corners of the images).
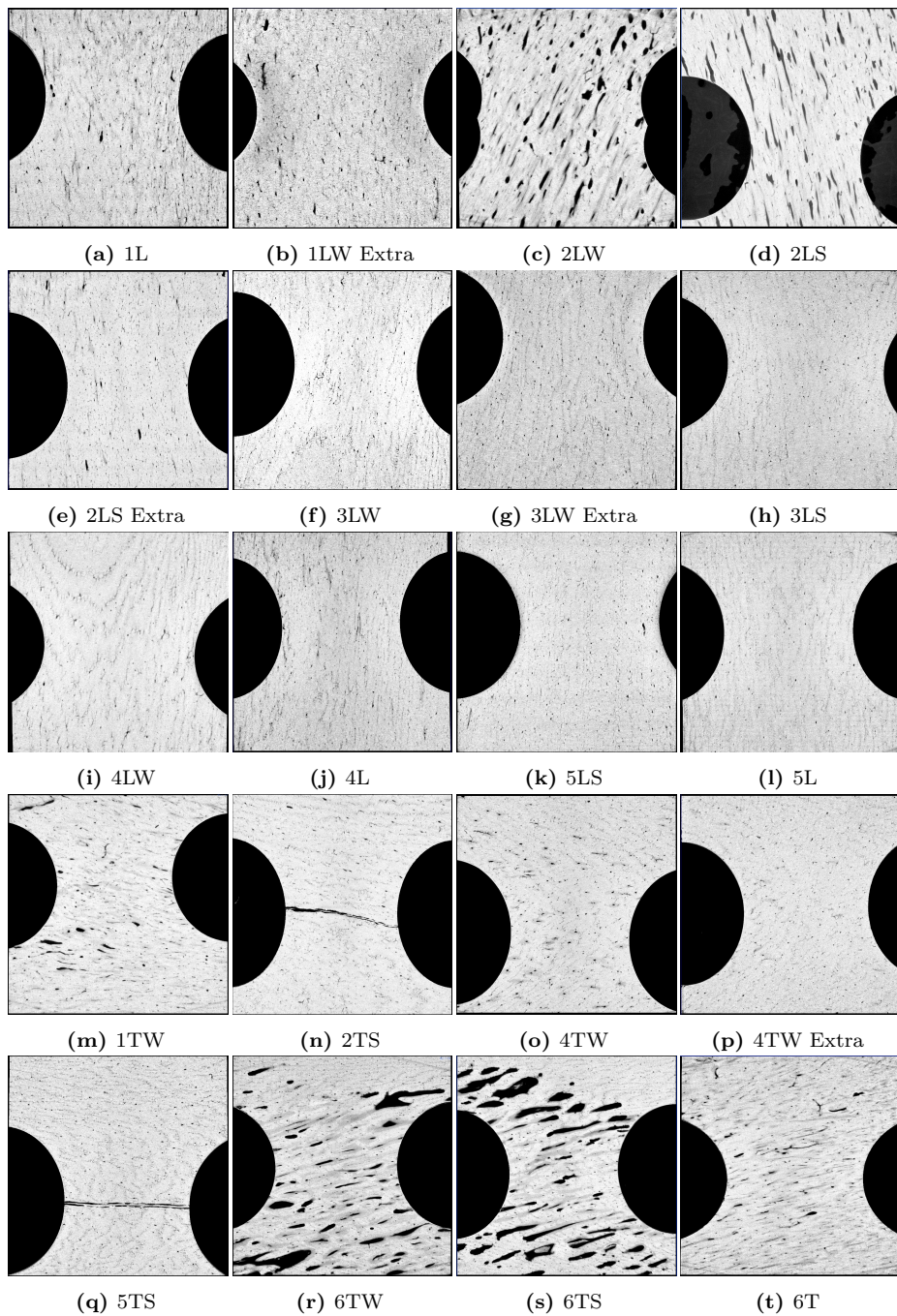
(a) 1L   **(b)** 1LW Extra   **(c)** 2LW   **(d)** 2LS

(e) 2LS Extra   **(f)** 3LW   **(g)** 3LW Extra   **(h)** 3LS

(i) 4LW   **(j)** 4L   **(k)** 5LS   **(l)** 5L

(m) 1TW   **(n)** 2TS   **(o)** 4TW   **(p)** 4TW Extra

(q) 5TS   **(r)** 6TW   **(s)** 6TS   **(t)** 6T

Figure 11: Coronal views of raw images from mid-slices of the 20 samples imaged during the second acquisition, each denoted by its ID. The differences in position is due to how the samples were stacked together in groups of five during the acquisition of the images.

In addition to the samples shown above, a small (about 1-1.5mm) slice from the middle of the 1TS sample (row 12 in Tab. 2) was extracted and imaged three times, each time at increasingly higher resolution (see Fig. 12) than the original sample (2.241μm, 1.240μm, and 0.600μm, compared to 9.25μm voxel size). This particular sample was chosen as its osteonal structure was very distinct. The 2.241μm resolution tomogram was used for validation. The idea being that supplying the segmentation pipeline with an easy-to-validate sample would be yet another way of validating the segmentation pipeline, both by visual comparison of the segmentations and the raw μCT images, and by volume comparison between the segmentations and structures segmented by manual outlining.
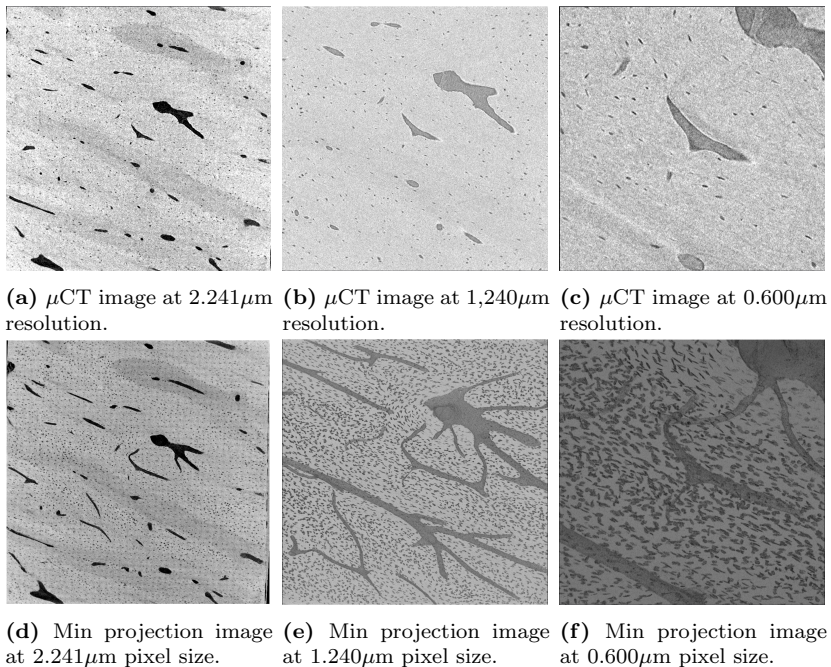

(a) μCT image at 2.241μm resolution. (b) μCT image at $1,240\mu$m resolution. (c) μCT image at 0.600μm resolution.

(d) Min projection image at 2.241μm pixel size. (e) Min projection image at 1.240μm pixel size. (f) Min projection image at 0.600μm pixel size.

Figure 12: High resolution μCT images from the 1TS sample. The position of the zoom-ins were chosen as the middle point of the previous field of view.

To achieve these higher resolutions the settings of the tomograph were altered in terms of sample placement, exposure time, energy, and power. The new settings, as well as the original ones, are seen in Tab. 3.

Table 3: Settings used to acquire the different pixel size tomograms.

Pixel size (μm)	Energy (kV)	Power (W)	Placement [S/D](mm)	Exposure time (s)	Binning
9.25	80	70	62/38	5	1
2.241	60	5	11/22	1.5	2
1.240	80	7	11/49	2	2
0.600	80	7	11/-	2	2

6.2 Extracting Geometrical Features

The pixel size (9.25μm) of the μCT images used in this projects enables visualisation of Haversian canals, osteons, interstitial bone, as well as non-Haversian canals, as is indicated in Fig. 13. As canals are hollow, no absorption of the X-rays will take place and hence regions corresponding to canals will show up as black in the images. Interstitial bone is highly mineralized and will hence absorb much of the incident X-rays, giving rise to bright areas in the images. Osteons have a lower mineral content than the surrounding interstitial bone, due to them being younger. Hence, intermediate gray areas surrounding the Haversian canals correspond to osteons. As is seen in Fig. 13 osteons are hard to distinguish in the μCT images used in this project. Also, regions inside the interstitial bone show the same gray scale as osteonal structures due to the inhomogeneity in mineralization of the tissue. In this project the segmentation was based on pixel intensity; a low intensity (black) was said to correspond to a canal, and a medium intensity (dark gray) was said to correspond to an osteon, while a high intensity (light gray to white) was said to correspond to interstitial bone.
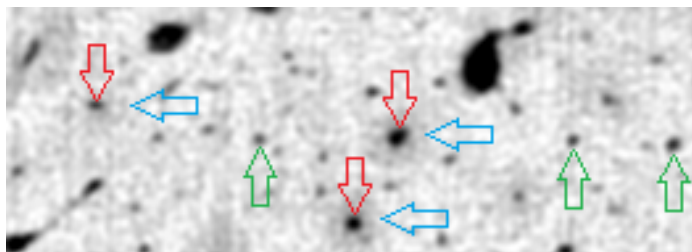

Figure 13: Cross section of part of one of the μCT images used in this project, illustrating the cortical histomorphology. Blue arrows denotes osteonal structures (darker gray). Red arrows denotes Haversian canals. Green arrows denotes primary vascular canals (non-Haversian canals). Light gray areas are interstitial bone.

6.2.1 Hardware and Software

The computer used for all processing and analysis has 64.0 GB of RAM, and an Intel(R) Xeon(R) CPU (E5-1620 v3) at 3.50 GHz. Pre-processing was done in ImageJ 1.51h [Schindelin et al., 2012; Schneider et al., 2012]. All code pertaining to the algorithms for segmentation and simplification were implemented in Matlab R2015b. Golden Standards for the segmentation were obtained by using Seg3D 2.4.0 [CIBC, 2016].
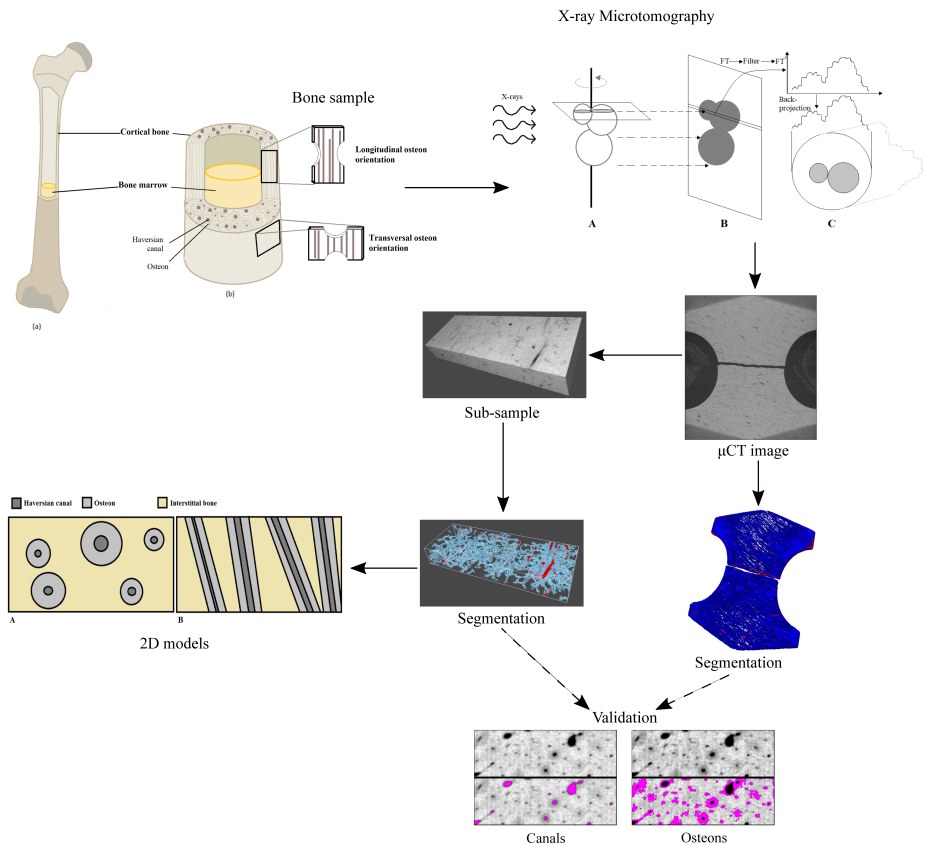
6.2.2 Image Analysis Pipeline

Figure 14: Flowchart overview of the different parts of this project.

In order to create a semi-automatic and user-friendly pipeline for extracting and analysing the microstructures in the bone samples (Fig. 14), Matlab code was written, aiming at implementing a small program. The initialization of the main program is shown in Fig. 15 where the user is given the choices to either segment a gray scale image or image stack, or to simplify a previously segmented image stack, or to validate a segmentation or simplification by overlaying the segmentation or simplification on top of the image stack used to create it. These options are explained further.
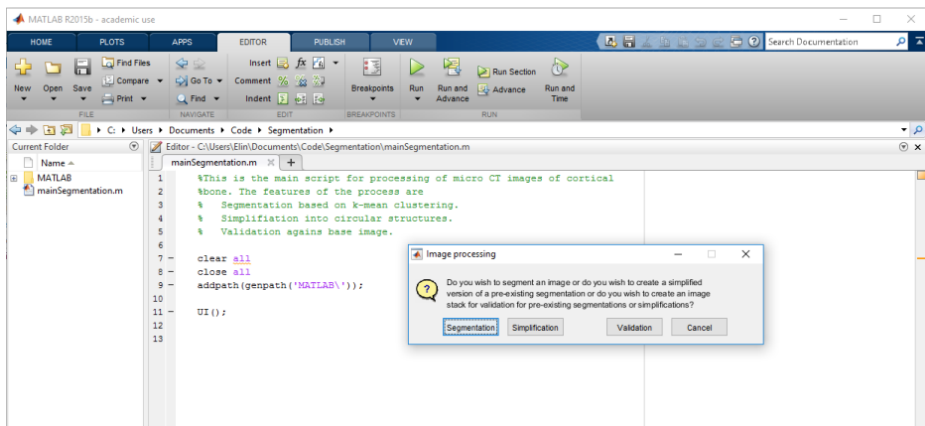

Figure 15: Initiation of the image analysis pipeline with user choices.

6.2.3 Pipeline for Segmentation

Fig. 16 shows two flowcharts of the pipelines implemented for segmentation.

User input:

- An image file for segmentation, whose directory and name is stored for future use, is chosen by the user.

- The user is asked if the images have been filtered using a Gaussian; if not the images will be filtered before further analysis is done.

- To determine whether or not background removal is necessary, the user is asked if the images are sub-samples, i.e. taken from within the sample volume, or if they contain background, i.e. if pixels exist

that are not part of the sample but of surrounding material used for packing the samples while in the tomograph.

- If, when looking at the finished segmentation, the user decides that the division of clusters into structures does not match well with the original image it is possible to specify the number of clusters to be assigned as canals and as osteons by changing the predefined numbers in the second user input prompt. This means that the entire segmentation process must be redone but it makes the result more adaptable to images with different gray scales.

- A final user choice of whether or not to create validation stacks is given; the method for creating these stacks is explained in section 6.2.5 Pipeline for Validation.

The resulting segmentations are saved as binary image stacks, of the same size as the input gray scale images, in a new folder, named *K-means*, at the directory of the original image file.
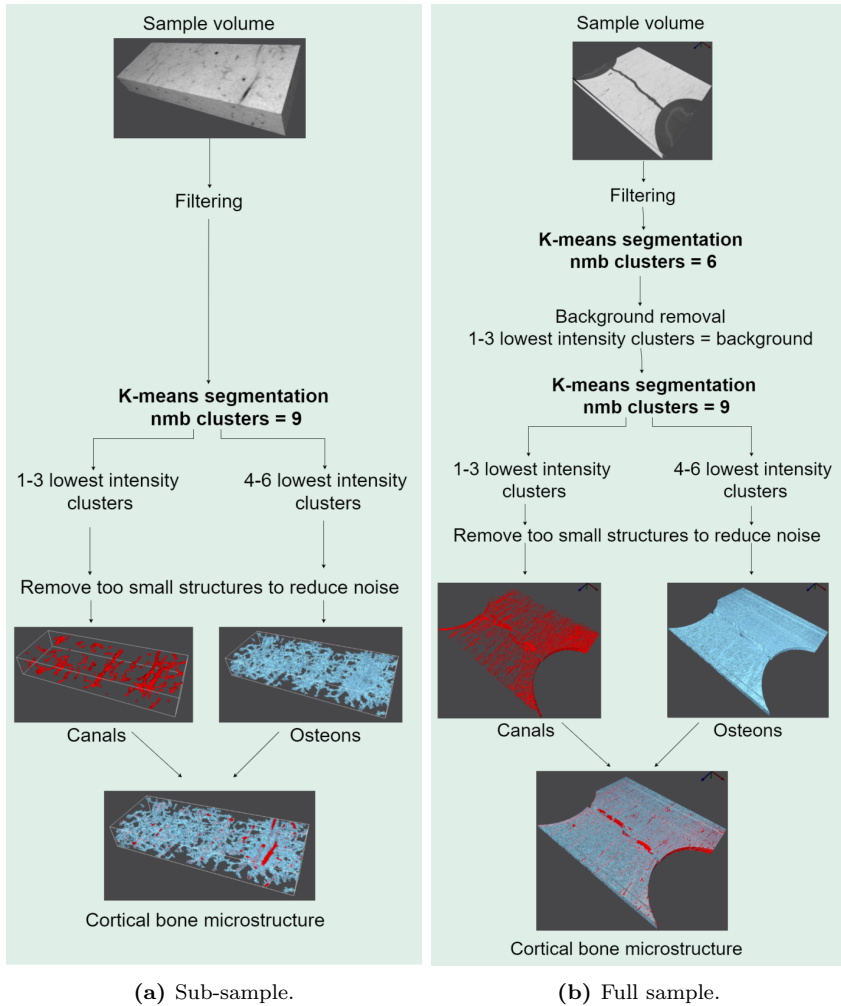
(a) Sub-sample.　　　　　　　**(b)** Full sample.

Figure 16: Flowcharts showing overviews of the pipelines implemented to analyse the sub-samples and the full samples. The number of clusters to use for the two segmentations (three each) was based on visual comparison of the segments and the μCT image.

6.2.4 Pipeline for Simplified Model

Based on the segmentations of the Haversian canals and the osteons, simplified models containing a number of structures were created by fitting cylinders to the placements (centres), orientations (tilts), and radii of the canals and osteons. The models were to be implemented in 2D as a transverse or longitudinal slice (see Fig. 17) of a sample, in order to enable

32

future implementation of finite element models to be used for validation of the results from the tensile tests.
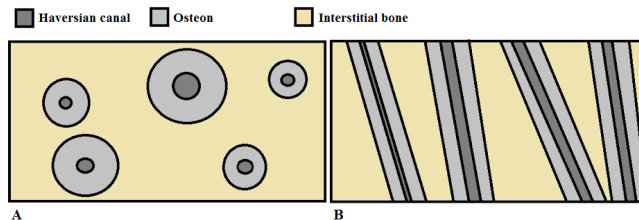

Figure 17: Idea for 2D model of osteons and Haversian canals. A Radial slice. B Longitudinal slice.

User input:

- The sample to be modelled is selected by the user, in the form of the two binary image stacks containing the segmentations of the microstructures. The directory and name of the image files is saved for future use.

- The desired number of structures in the resulting model is chosen by the user as 5, 10, or 15; the idea being that a manageable number of structures were to be modelled, irrespective of the gross size of the input. If too many or not enough structures are found, the user will be asked whether or not to remove or add structures in the final model.

- The final user input to the pipeline is whether or not to overlay binary images, representing the fitted cylinders, on top of the corresponding segmentations. If this is desired, additional image stacks are created and saved in a new (or present since the previous segmentation) folder named *Validation*; the method for creating these stacks is explained in section 6.2.5 Pipeline for Validation.

The resulting models are saved in form of text files, containing the center points and radii of all fitted cylinders, and as binary image stacks of the cylinders, of the same size as the input gray scale images, in a new folder, named *K-means*, at the directory of the original image file.

6.2.5 Pipeline for Validation

A simple method of validating the segmentation or the simplified model was implemented in order to get a quick and easy overview of the results of the pipeline.

User input:

- The user chooses one binary image file, containing cylinder structures or segmentations, and one gray scale image file, containing the corresponding μCT image. The file name of the μCT image as well as its directory are saved for future use.

- The user is warned against having any active Windows File Explorer windows as Matlab will not be able to save the segmentations correctly in that case.

The binary images are used as masks that are overlaid, in magenta, on top of their corresponding gray scale image. The validation image is placed underneath the μCT image (see Fig. 18) in order to simplify the visual validation.
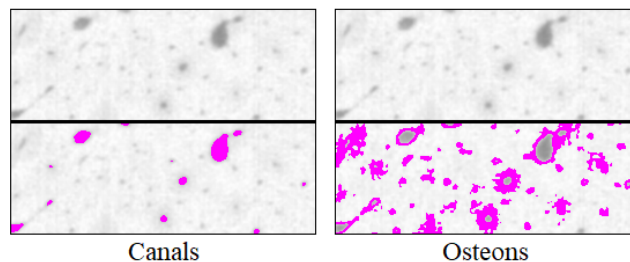

Figure 18: Overlay for validation. A segmentation of canals and osteons have been overlain on top of the corresponding μCT image.

If the program encounters any problem the program will terminate and a prompt window will let the user know that something went wrong. If there are no issues in the pipeline the Matlab command window will give status and time updates when segments of the pipeline is passed.

The resulting validations are saved in a new folder, named *Validation*, at the directory of the original image file.

6.2.6 Pre-processing of the Micro CT Images

In order to enhance the microstructural elements in the μCT images a Gaussian filter followed by a mean filter was applied to all images in all sub-stacks. Fig. 19 depicts the difference between a raw μCT image and filtered μCT images. The filtering was done in ImageJ [Schindelin et al., 2012; Schneider et al., 2012] using the plugin *Smooth (3D)* [Ferreira and Rasband, 2012] with a σ of 0.8 for the Gaussian filter and the built in mean filter with a radius of 1 pixel[6]. Using one filter only was tried for both filters, separately, but it was deemed best to apply both in order to get a sharp yet smooth segmentation without too much noise. In the Matlab program that was developed a filter possibility was added in order to facilitate for un-filtered images; this filter, *imgaussfilt.m* which uses a square kernel in 2D when σ is given as a scalar, was a Gaussian, with the same σ as previously, and gave identical results as the double filter applied using ImageJ.
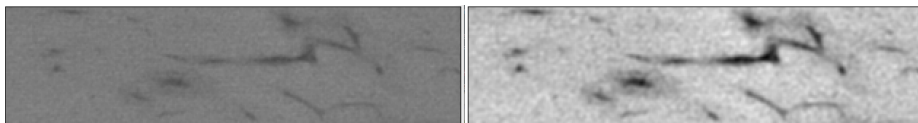

Figure 19: Raw μCT image (left), and filtered (right). The filtering enhances the microstructure.

Segmenting an entire image stack in order to analyse the overall distribution and architecture of the microstructures required removal of background consisting of μCT signal from wet gauze that was wrapped around each sample in order to keep them moisturised. This background removal step was not necessary if the sample to be segmented was *virtually* cut out from within the bone volume.

Removing the background was done based on an initial K-means clustering of the pixel intensities into six partitions. This clustering was only done once even though the resulting segmentation was at risk of being based on a local minimum and not a global one (see section 5.3.1 Segmentation using K-means clustering), the reasoning being that the eventual crudeness would not be a problem.

---

[6]The kernel size was chosen based on [Maggiano et al., 2016], and the radius of the mean filter was chosen based on visual examination of the resulting images.

The background, defined as the four clusters corresponding to the lowest pixel intensities (through trial and error), and a binary mask was created based on these four clusters. However, some canal structures were clustered together with the background since their pixel intensities were the same as the those of the background.

By morphological operations (see Fig. 21) the mask was altered to cover only the actual background. The mask was enlarged slightly in order to remove the edges of the bone sample as the edge pixels were "shadowed" by the background, i.e. their intensities were lower than what was actually representable for the tissue and would hence cause artefacts in the subsequent segmentation which reduced visibility of the microstructures below the edges.
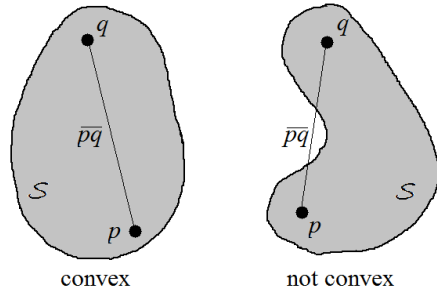

Figure 20: A set, $\mathcal{S}$, (gray) is convex if the line segment $\overline{pq}$ between any pair of points $p, q \in \mathcal{S}$ is completely contained in $\mathcal{S}$.

To get rid of unevenness of the mask edges the mask was smoothed by using the Matlab function convhull.m [MathWorks, 2017], which returns the 2D convex hull of the data points given to the function. The convex hull, $\mathcal{CH}(\mathcal{S})$, of a set, $\mathcal{S}$, is the intersection of all convex sets containing $\mathcal{S}$ [de Berg et al., 2008]. A set is said to be convex if the line segment $\overline{pq}$ between any pair of points $p, q \in \mathcal{S}$ is completely contained in $\mathcal{S}$, as is illustrated in Fig. 20.

If a pixel in the original image was determined to be part of the background, i.e. if the binary mask covered the pixel in question, its intensity was altered from its original low value to the infinite intensity[7]. This caused the background to be clustered together with pixels corresponding to interstitial bone, during the subsequent re-clustering. As interstitial bone was of no interest to the segmentation these clusters were

---

[7]It was also tested to use the maximum intensity in the original μCT image, or the maximum intensity of all pixels in all images. However, in most images this resulted in the background pixel intensity diverging too much from the intensities of the interstitial bone for the following clustering and division into structures to work properly. Instead pixels corresponding to interstitial bone was clustered together with osteonal pixels resulting in a faulty segmentation.

disregarded after the actual segmentation and hence the background was removed.

The operation to smooth the mask edges (taking the convex hull of the mask) caused the height of the mask to differ between images, resulting in segmentations with jagged surfaces (see Fig. 22). As this impeded the visual analysis of the segmentations a workaround was implemented in that the resulting gray scale image stack, with background removed, was trimmed so that the upper and lower edges of all images were the same. This removed the vast amount of the background, reducing the impact of its infinitely bright pixels on the subsequent clustering.

Figure 21: Binary mask (white) used for background removal. The crude mask is composed of the four clusters corresponding to the lowest pixel intensities after K-means clustering of the original gray scale image using six clusters.
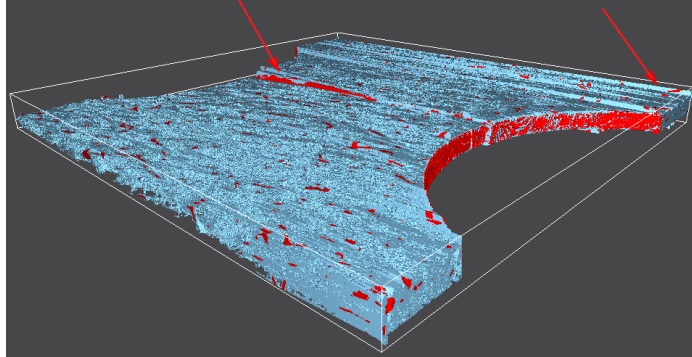
Figure 22: Jagged surface (ridges indicated with red arrows) in final segmentation, due to differences in the masking of each individual image. The blue ISO surface represents the segmentation of osteonal structures. The red ISO surface represents the segmentation of canals.

6.2.7 Method for Segmentation

The method chosen for segmenting the μCT images was K-means clustering (see details in section 5.3.1 Segmentation using K-means clustering). This method was chosen since the information given in the μCT images is pixel intensity, which is based on the absorption of the microstructures in the bone samples. Since different microstructures have different intensities in the images, clustering pixels based on their intensities will separate the different microstructures from each other, enabling a segmentation of the structures of interest. The clustering is repeated three times in order to try to avoid the solution being a local minimum rather than a global one.

If no background is present in the image/images all pixels are used simultaneously in K-means clustering, using the function kmeans [MathWorks, 2016a], to segment out the microstructures, as shown in Fig. 16b. The input given is a 1D array, comprised of all pixel values in the image set to be segmented, the number of clusters, into which the pixel values were to be partitioned, and the number of times to replicate the clustering (three). By default the kmeans function determines the partitioning based on the squared Euclidean distance between the centres and the data points (here the pixel intensities), and uses the K-means++ algorithm to initialize the center positions of the clusters. Fig. 23 shows the clustering of a gray scale image, and the subsequent division of clusters into segments.
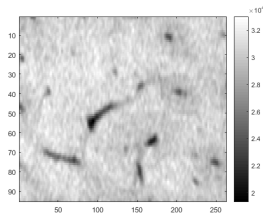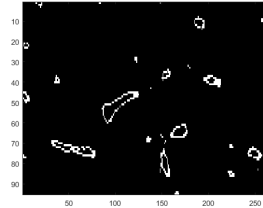
(a) Filtered μCT image.
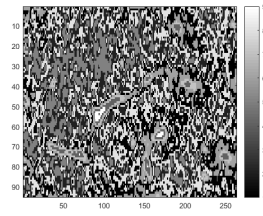
(b) K-means clustering of Fig. 23a.
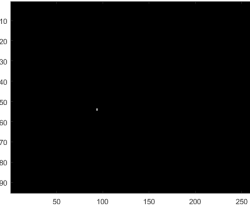
(c) Lowest pixel intensities.

(d) Fourth lowest pixel intensity.
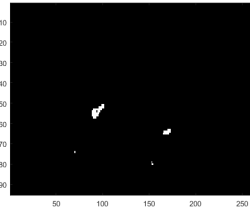
(e) Second lowest pixel intensities.
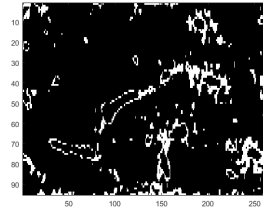
(f) Fifth lowest pixel intensity.
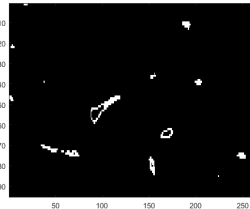
(g) Third lowest pixel intensities.
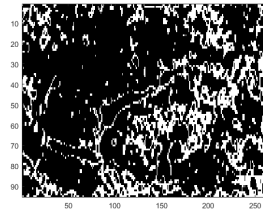
(h) Sixth lowest pixel intensity.
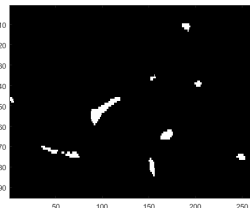
(i) Final canal segmentation.
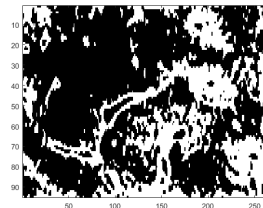
(j) Final osteon segmentation.

Figure 23: Explanatory illustration of how K-means clustering of the different pixel intensities, is used to segment microstructure in μCT images. First, second, and third lowest pixel intensities correspond to canals. Fourth, fifth, and sixth lowest pixel intensities correspond to osteons.

39

If background is present the pipeline is different, as shown in Fig. 16a. The background removal process is described in the previous section 6.2.6 Pre-processing of the μCT Images. After the background removal the pipeline merges with that of the sub-samples as the image/images is/are clustered again, now using nine clusters, and the same division of clusters into structures are made.

Structures below a certain volume threshold (100 voxels for canals, and 2000 voxels for osteons) are removed in order to reduce noisiness in the final segmentations.

The resulting segmentations is then saved as binary image stacks of the same size as the input gray scale images in a new folder, named *K-means*, at the directory of the original image file.

6.2.8 Method for Simplified Model

The data needed in order to create a simplified model of the microstructure were centers, radii, and tilts.

6.2.8.1 Finding the Tilts and Center Points

Finding the average orientation for each canal structure was done by constructing a binary 3D matrix out of the images and then looking at each canal, now represented as 3D points, individually and performing principal component analysis (PCA) to determine the direction of largest spread (Fig. 24a, [Bishop, 2009]).

Principal component analysis was performed using the Matlab function pca.m, [MathWorks, 2016b], which returns the coefficients and scores of the principal components of the 3D coordinates corresponding to a segmented canal structure. Using the coefficients and scores corresponding to the largest principal component, the endpoints of the vector representing the main orientation of the canal structure (see Fig. 24b) were obtained. The endpoints were used to obtain an orientation vector for each canal in the sample. A mean orientation for the entire sample was then calculated and used to determine whether or not the 3D matrix, containing only the structures large enough to be of interest[8], needed to

---

[8]Structures smaller than 50 pixels were omitted.

be re-sliced[9] in order to facilitate for a later step in the simplification pipeline, where circles are fitted to the structures in each image in order to obtain radii for the Haversian canals and the osteons. If re-slicing was deemed necessary both the new 3D matrix containing canal structures and the original 3D matrix containing osteonal structures were re-sliced in the same manner.
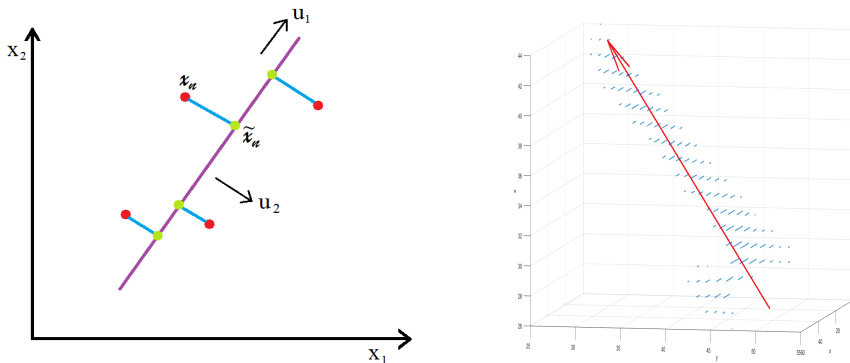
(a) Given a set of data points (red dots) PCA aims at finding a space (magenta line) of lower dimensionality than that of the data such that the projection (green dots) of the data onto this space maximizes the variance of the projections. Alternatively, PCA can be defined as minimizing the sum-of-squares of the projection errors (blue lines). u_1 signifies the direction of largest spread for the data points. u_2 signifies the direction of least spread for the data points.

(b) The vector (red) corresponding to the largest principal component of the data points in the canal structure (blue). Since the coordinates of the data points representing a canal in a binary 3D matrix have a spread that is largest in the direction of the canal, PCA can be used to estimate the direction of the canal.

Figure 24: Description of PCA in 2D, shown in (a), and use of PCA in 3D in this project, shown in (b).

The Haversian canals are interconnected via the lacuno-canalicular network (LCN). In order to fit cylinders to each individual canal the LCN-branches in between them needed to be removed in order to separate the canals for individual analysis.

---

[9]Samples labelled L had microstructures running in the depth direction of the stack of images, i.e. the images were taken in the plane transverse to the orientation of the microstructures, whilst the samples labelled T had microstructures running across the images in the stack, i.e. the images were taken in the plane parallel to the orientation of the microstructures. Samples with the latter orientation had to be re-sliced in order to have the same orientation as the former.

This was done by, again, looking at each separate connected component above a certain threshold (50 voxels) and evaluating its principal components. A canal structure was unbranched if its orientation was cohesive[10] with the mean orientation of the sample.

If a canal structure was deemed cohesively oriented its data points were saved in a cell in a structure created for storing data points corresponding to individual canals for later use, and the endpoints of the structures principal component were stored in a $M \times 3$ array, where M was the number of canals large enough to be of interest in the sample, to be used as coordinates for the centres of the top and bottom of the cylinders to be fitted to the canals and osteons.

If the spread of the canal structure indicated branching it was processed in order to remove branches. This was done by looking at 2D slices of the structure, in each of its three dimensions (see Fig. 25). The structure was sliced so that the 2D images were of the xy, yz-, and xz-planes (Fig. 25c-e). Each 2D structure in each sequential slice was analysed based on roundness as a measure on if the structure was a canal or a branch[11]. The circularity of a structure was measured using Eq. 6, where a value of c close to one means the object is round. The threshold (i.e. the value of c necessary for an object to be considered round) used in the pipeline was 0.4 in the xy-plane, and 0.2 in the yz-, and xz-planes.

$$c = 4\pi \frac{area}{perimeter^2} \qquad (6)$$

If a 2D structure was deemed to be a branch the data points were changed from one to minus infinity. All data points in the 3D matrix with value less than zero were then set to zero, resulting in the removal of branches.

---

[10]By looking at the ratio between the second largest and the largest principal component, as well as the ratio between the third largest and the largest principal component, the spread of the canal structure could be evaluated. If this ratio was less than 0.4 the structure was deemed as not branched, and vice versa.

[11]In the xy-plane a canal would be more circular and a branch would be more oval.
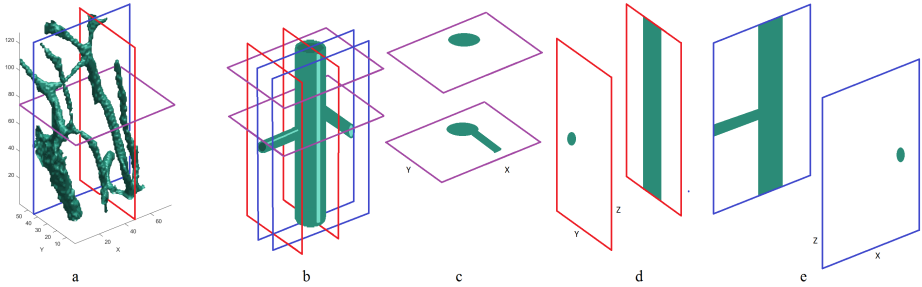
Figure 25: Branch detection in different planes, based on roundness. (a) ISO surface showing segmentation of branched canal cluster. (b) Principle sketch of canal with branches, overlaid with slicing planes. (c) Slicing in the xy-plane results in circular structures for the canal and non-circular structures for branches. (d) Slicing in the yz-plane results in circular structures for branches protruding in the x-direction, and non-circular structures for the canal. (e) Slicing in the xz-plane results in circular structures for branches protruding in the y-direction, and non-circular structures for the canal.

However, this process resulted in the removal of junctions between the branches and the canal and hence the remaining canals were discontinuous. In order to find the actual number of canal structures in the sample, and not look at each disjointed piece individually, all canal pieces from the 3D matrix were plotted in a common figure, each piece having an individual colour (see Fig. 26b). User input was then gathered in terms of which canal pieces fit to the same canal. The user indicated pieces seeming to form a common canal by clicking on them until all pieces corresponding to a certain canal had been marked. The 3D coordinates of the indicated data points were saved into a common cell in the cell structure created to store data points corresponding to individual canals. The structures were removed from the figure, and PCA was run on all data points giving the endpoints of the principal component which were stored as the centres for the top and bottom of the cylinder to be fit to the canal. The user continued to indicate common canal structures until the remaining structures could not be considered corresponding to canals or there were no structures left. Then the next structure was analysed, and if this structure was deemed to be branched the procedure was repeated.
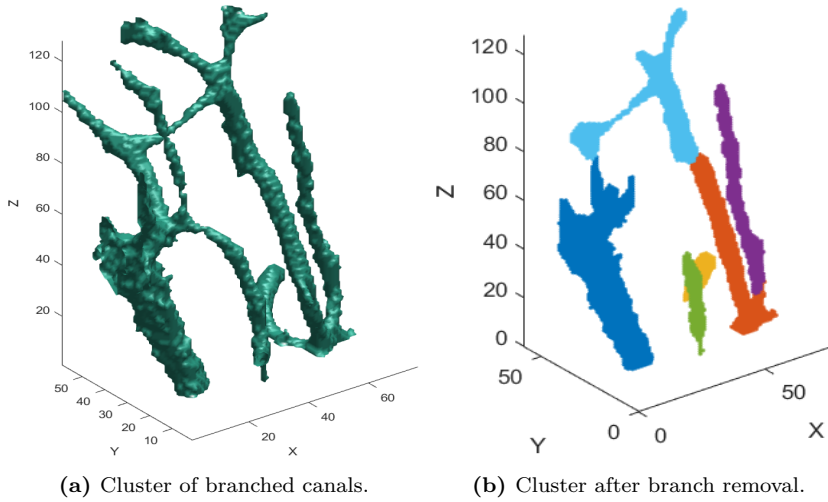
43

(a) Cluster of branched canals.   (b) Cluster after branch removal.

Figure 26: Due to the LCN some canals were clustered together, making analysis of individual canals impossible. Removing branches improved the analysis.

When all structures in the main sample had been analysed and all true canal structures had been extracted and saved, data extracted from branched structures were converted from 3D coordinates into binary matrices representing the canal structure.

6.2.8.2 Finding the Radii

To obtain radii for the Haversian canals and osteons circles were fitted to the structures in the binary images. This was done by analysing each canal structure in the cell structure constructed in the previous stage in 2D (in the xy-plane) and fitting circles to the structures. The circles were fitted using the Matlab function fitcircle.m [Brown, 2007] which fits a circle to a set of 2D points and returns the center coordinates and the radius.

When circles had been fitted to all structures in one slice of the canal matrix the same slice in the osteon matrix was analysed. As osteons surround Haversian canals the structures corresponding to osteons were hollow; using the Matlab function imfill.m [MathWorks, 2006] holes were filled. Osteonal structures at the edges of the slice needed to be treated separately as any holes inside such structures could not be filled using the imfill.m function due to the edge straddling. Each such edge structure

44

was found and depending on what or which of the edges of the slice the structure straddled, a border of pixels was added onto the structure after which filling the holes was possible. The border was then removed again.

The canal slice was then used as a mask to find which canals had osteonal structures surrounding them and which were in fact pores, and hence of no interest. If a canal was deemed to be a pore its data points in the slice were set to zero and its data regarding radius was not used.

If a canal was deemed an actual Haversian canal its radius was saved; in this way radius r fitted to canal a was saved at index s, which indicated in which slice the radius was fitted and hence the distribution of the canal through the sample could be tracked.

To fit a radius to an osteon surrounding a specific canal the radius of that canal was used to fit a circle which was superimposed ontop of the osteon. The radius was increased in steps of one pixel until a set number of the pixels on the circle were superimposed onto pixels outside of the osteonal structure. This radius was then saved in the same way as the radii of the Haversian canals.

6.2.8.3   Fitting Cylinders

Based on the center points for the beginning and end of each canal and corresponding osteon, determined using PCA, and the corresponding radii, determined by the fitting of circles, a 3D model was created where cylinders were fitted to the microstructures.

In order to use this model for finite element simulations it was converted into 2D by looking at one transverse (in the xy-plane) and one longitudinal (in the xz-plane) slice.

The transverse slice was taken as the base of the 3D model and was implemented by using the center point x- and y-coordinates and radii of the structures present in this slice.

If the number of structures found, X, in this slice was less than the user requested number (5, 10, or 15) the user was asked if the lesser number was still okay or if structures (requested number minus X) should be added. If Y structures were to be added a random set of Y center coordinates, inside the interval defined by the minimum and maximum x-coordinates of the existing centres, was added to the set of centres. In

the same manner Y radii for the osteons and for the Haversian canals were added to the existing radii. If instead the number of structures found, X, was larger than the requested number the user was asked if modelling all structures was desired or if Y structures were to be removed. If structures were to be removed, Y random center coordinates with their corresponding osteonal and canal radii were removed.

The longitudinal slice was created based on the structures present in the transverse slice. Using the top and bottom center point x- and z-coordinates for the cylinders fitted to these structures as well as the corresponding radii, a longitudinal model could then be implemented.

6.2.9 Method for Validation

Three methods of validation were used, as described below, and implemented on the six samples that contained true osteonal structures.

6.2.9.1 Visual and volume comparison between structures segmented using the implemented pipeline and structures segmented manually

Manual segmentation was performed in Seg3D on a subsample from the Extra 2SL sample as well as on the 2.241μm voxel tomogram of the 1TS sample. The segmentation was done by identifying and outlining microstructures, based on their shape and gray scale. The difference compared to threshold based segmentation is the shape consideration; in thresholding any pixel within the intensity interval will be clustered to a certain segment, independent of its placement in the image and hence the shape of the object it belongs to. Fig. 27 shows the resulting segmentation. Again, the segmentations were used for visual comparison with the K-means segmentation in Seg3D, and for analytical comparison, by comparing the number of pixels in the manual threshold segmentation to the number of pixels in the corresponding K-means segmentation (i.e. the volume fraction) to get a measurement of differences in volume.
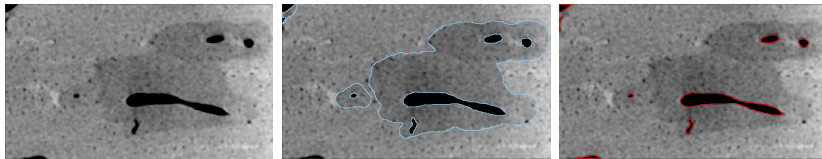
(a) Filtered μCT image. (b) Outlines of osteons (blue). (c) Outlines of Haversian canals (red).

Figure 27: Example of hand segmented microstructures in the 1TS sample imaged with 2.241μm voxel size.

6.2.9.2 Visual comparison between structures segmented using the implemented pipeline and structures in the corresponding μCT images

To have a quick and easy method for validating the K-means segmentation, each segmentation of each image stack was overlaid onto the corresponding μCT image and inspected in Seg3D and in ImageJ. This was done in order to determine how well the segmentations overlapped their respective structures in the original image.

6.3 Structure Sizes and Porosity

The sizes of the structures in each of the six osteonal samples was estimated using the ImageJ function Thickness in the plugin BoneJ [Doube and et al., 2010]. The function takes a binary image stack, with the particles to be analysed being the foreground (255). The thickness at a point p is defined in the function as the diameter of the largest sphere that can fit within the structure and that contains the point p.

The porosity of all samples was estimated using the ImageJ function Volume Fraction in the plugin BoneJ. The function takes a binary image stack, with the particles to be analysed being the foreground (255), and can be used in two ways; the one used here is voxel-based and calculates porosity as the number of voxels representing holes or pores divided by the total number of voxels in the image.

7 Results

7.1 Segmentation

It was discovered that six of the 13 samples imaged the first time and eight of the 20 samples imaged the second time contained no or very little osteonal structures. It is believed that these samples were collected from the anterior region of the femur as Haversian systems are mainly confined to posterior regions of bovine femurs [Mayya et al., 2016]. Only eight samples showed to be osteonal cortical bone, i.e. containing osteonal structures; these are listed in Tab. 4. The samples 6TW and 6TS were omitted from analysis of osteonal structures as their pore size was extremely large and not representative of normal cortical bone. Due to canals large enough to permeate the entire thickness of the samples the segmentation failed (see discussion in section 8.1 Segmentation). The samples were, however, still used for porosity analysis.

Table 4: Sample ID, and presence of osteonal structures.

ID	2LW	2LS	4LS	1TW	1TS	6T	6TW	6TS
Osteonal bone	Yes	Yes	Yes	Yes	Yes	Yes	Yes (large)	Yes (large)

Fig. 28 shows images of segmentations of the microstructures in one subsample from two representative samples of the six osteonal bone samples (see Appendix 2 for overlays of all osteonal samples). The number of clusters used for each segment is three.

(a) Canals, 2LW.   **(b)** Osteons, 2LW.

(c) Canals, 2LS.   **(d)** Osteons, 2SL.
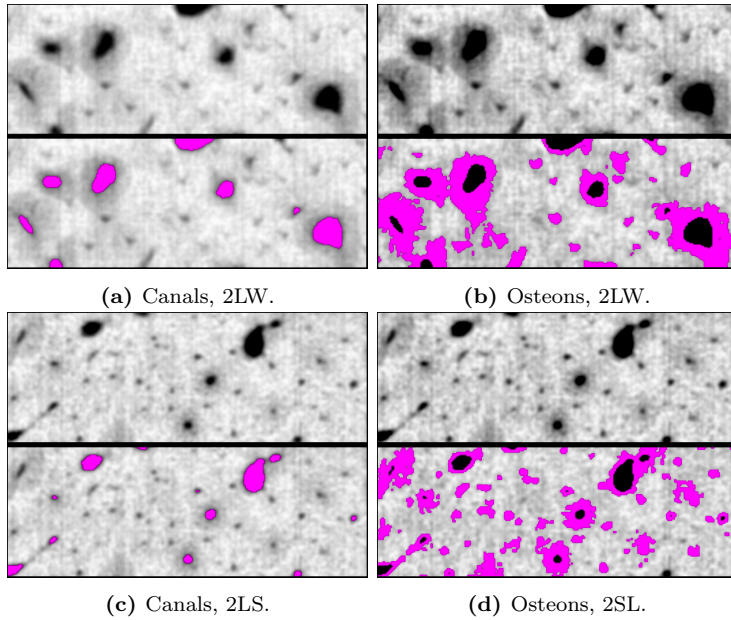
Figure 28: Segmentations of sub-samples from the six osteonal bone samples. The segmentation has been overlaid (magenta) on top of the original μCT image.

Fig. 29 shows the segmentation of one sub-sample from a non-osteonal bone sample. The number of clusters used for each segment is three.

(a) Canals.   **(b)** Osteons.
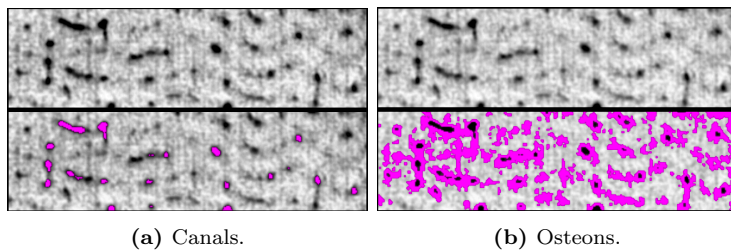
Figure 29: Segmentations of sub-samples from one of the bone samples which did not contain osteonal structures. The segmentation has been overlaid (magenta) on top of the original μCT image.

Fig. 30 shows the ISO surfaces of the segmented microstructures from one sample. In this case background has been removed in order to visualize the internal structure of the sample.
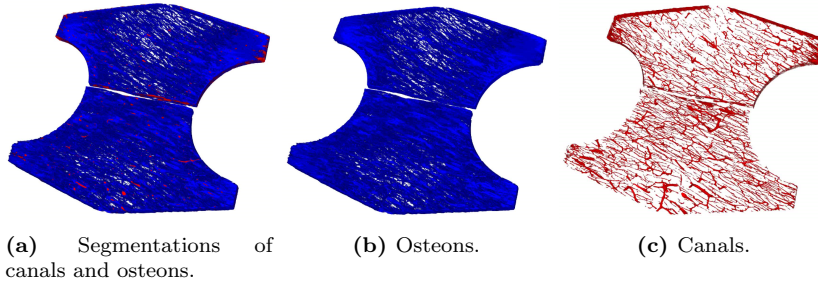
50

(a) Segmentations of canals and osteons.   **(b)** Osteons.   **(c)** Canals.

**Figure 30:** Segmentations of one transverse sample.

7.1.1 Validation

7.1.1.1 Visual and volume comparison between structures segmented using the implemented pipeline, and structures segmented manually:

Fig. 31a shows comparisons between the volumes of the segmentations done using the implemented segmentation pipeline, and segmentations done manually. For the lower resolution (9.25μm) images the manual segmentation of both Haversian canals, and osteons covers larger areas and hence gives a higher segmentation volume, see Fig. 32a. This issue could be alleviated by increasing the number of clusters used as the two segments, i.e. using four clusters each for the osteons and the canals, instead of the default three. The result of K-means clustering using four clusters as canals and the following four clusters as osteons is shown in Fig. 32c. For the higher resolution (2.241μm) images the behaviour is the opposite, with the manual segmentation covering less area and hence less segmentation volume, see Fig. 32e. In this case this is due to the enhancement of microstructure in the sample; small pores are picked up as canals by the K-means pipeline, and microstructure in the interstitial bone is picked up as osteonal tissue. For the segmentation of canals, the issue could be resolved either by removal of particles below a certain threshold, resulting in removal of small pores, or by reducing the number of clusters used as canals by one, i.e. from three to two. The result of K-mean segmentation using two clusters as canals and the following three clusters as osteons is seen in Fig. 32f .

51
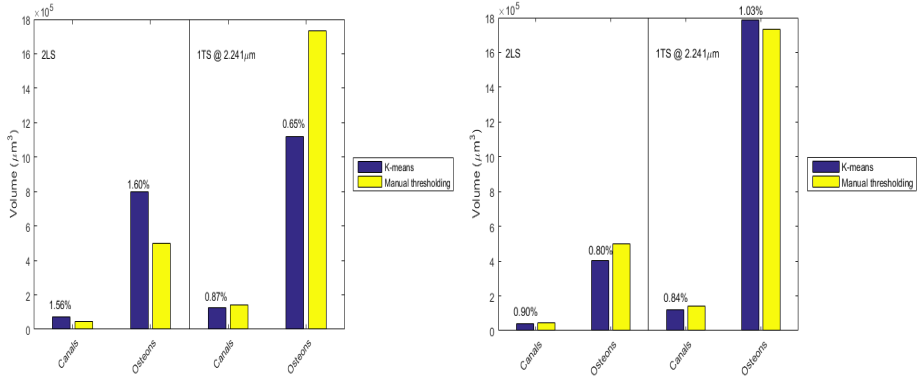
(a) Three clusters each used as canals, and osteons.

(b) Four clusters each used as canals, and osteons in Extra 2SL. Two clusters used as canals, and three as osteons in T1S.

Figure 31: Volume comparison between segmentations done using the K-means pipeline, and manual segmentation. The error percentage is reduced by the change of number of clusters used.
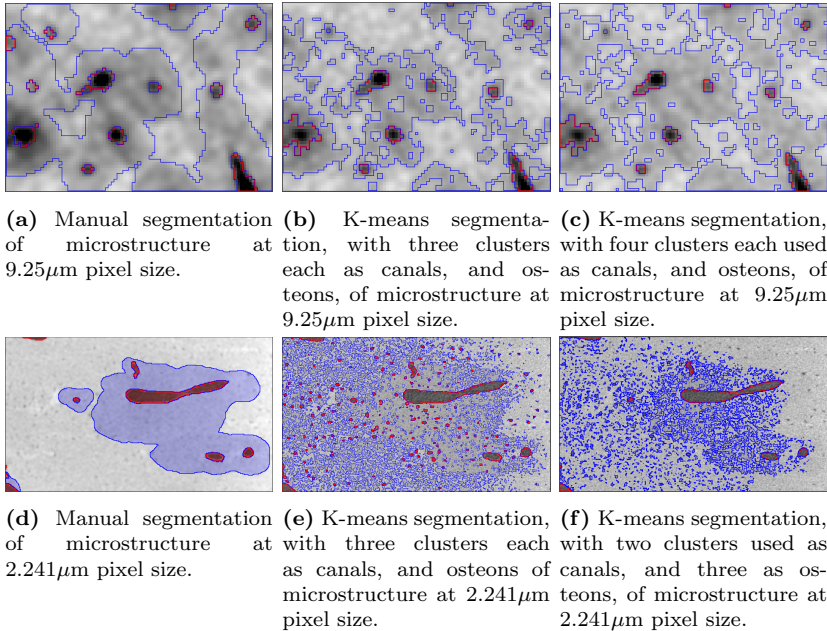
(a) Manual segmentation of microstructure at 9.25μm pixel size.

(b) K-means segmentation, with three clusters each as canals, and osteons, of microstructure at 9.25μm pixel size.

(c) K-means segmentation, with four clusters each used as canals, and osteons, of microstructure at 9.25μm pixel size.

(d) Manual segmentation of microstructure at 2.241μm pixel size.

(e) K-means segmentation, with three clusters each as canals, and osteons of microstructure at 2.241μm pixel size.

(f) K-means segmentation, with two clusters used as canals, and three as osteons, of microstructure at 2.241μm pixel size.

Figure 32: Segmentations overlaid on top of their corresponding μCT image.

7.1.1.2 Visual comparison between structures segmented using the implemented pipeline, and structures in the corresponding μCT images:

Fig. 33 shows the K-means segmentations of canals and osteons, for two representative samples (4LS, and 1TW), overlaid on top of their original μCT image. The exact same segmentation setting were used on both samples.

(a) Canals in the first substack from 4LS. **(b)** Osteons in the first substack from 4LS.

(c) Canals in the first substack from 1TW. **(d)** Osteons in the first substack from 1TW.
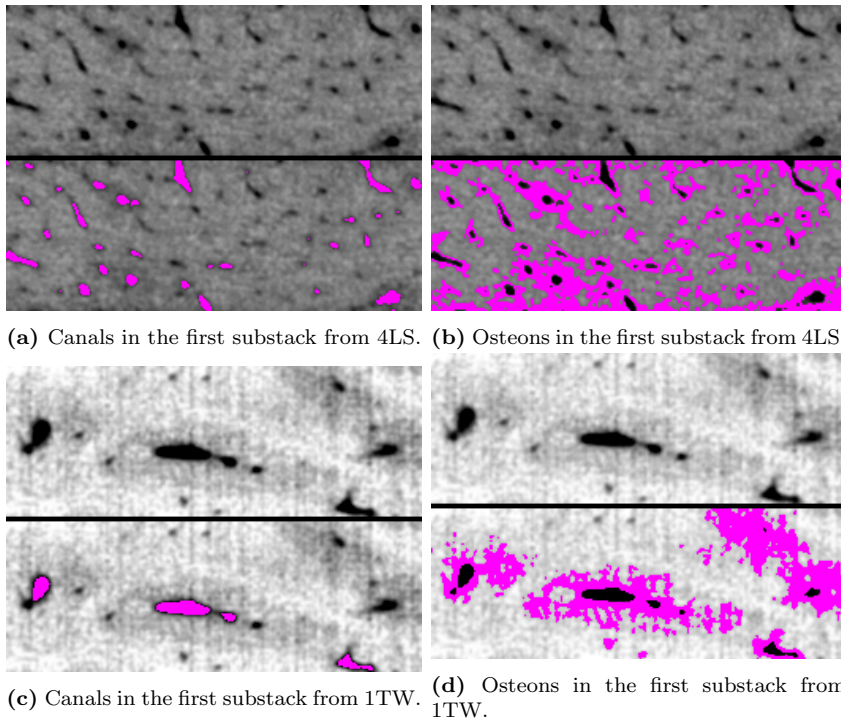
Figure 33: Segmentations overlaid on top of their corresponding μCT image. The difference in gray scale in the μCT images between the samples is due to the different acquisition occasions.

7.1.2 Structure Sizes and Porosity

The mean thickness, with corresponding standard deviation, of the osteons and the Haversian canals are shown in Fig. 34a. Fig. 34b shows the maximum thickness for the microstructures in the samples.

(a) Mean thickness.

(b) Max thickness.
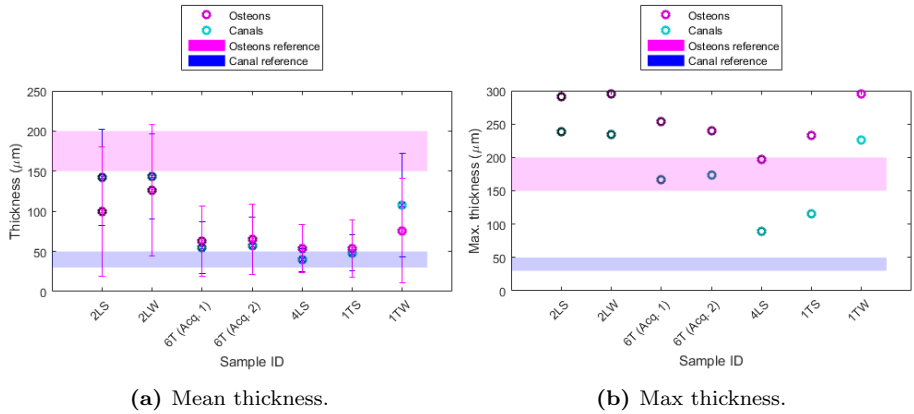
Figure 34: Calculated mean, and max diameter (circles) with standard deviation (bars) compared to values mentioned in literature; osteons: 150-200μm (179μm, [Budyn et al., 2010, 2012]; 192.7μm, [Zhang et al., 2014]; 200μm, [Carnelli et al., 2013]); Haversian canals: 30-50μm (30μm, [Zhang et al., 2014]; 37μm, [Budyn et al., 2010, 2012]; 50μm, [Carnelli et al., 2013]). The values are the mean of the calculated diameters for both subsamples corresponding to the same sample.

The porosities for the osteonal samples are shown in Tab. 5. Porosities for all samples are shown in Fig. 35.

Table 5: Porosity in percent of total bone volume for each of the two subsamples of the ten bone samples.
*Acquisition 1. **Acquisition 2.

	2LS	2LW	6T*	6T**	4LS	1TS	1TW
Subsample 1	4.5	5.3	2.8	2.5	3.5	2.2	3.8
Subsample 2	6.7	7.4	3.4	2.5	3.5	2.8	3.5
Mean	5.6	6.4	3.1	2.5	3.5	2.5	3.7

54
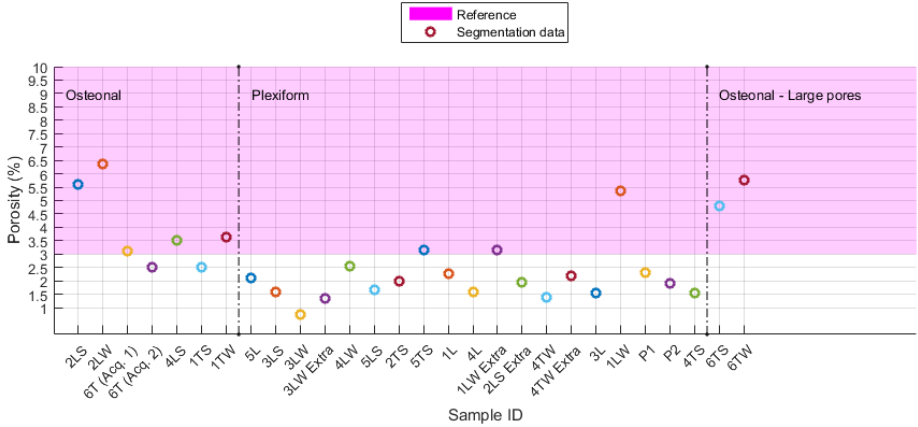
Figure 35: Calculated porosity (circles) compared to values mentioned in literature, 3-10% (3.79% [Budyn et al., 2010, 2012]; 5-8% [Manilay et al., 2013]; 5-10% [Lee et al., 2012]). The values are the mean of the calculated porosity for both subsamples corresponding to the same sample.

7.2 Simplified Model

Fig. 36 shows ISO surfaces representing the segmented canals in one sub-sample. In 37 the corresponding 3D model, i.e. cylinders (magenta/-cyan) fitted to the canals and the osteons, are overlain on top of the ISO surfaces. Fig. 38 show 2D models based on the 3D model.

The average estimated diameters for Haversian canals and osteons was 78μm, and 226μm, respectively. This correlates with literature (30-50μm, and 150-200μm), and with the average diameter of the segmented structures (85μm for canals, and 129μm for osteons).

(a) View 1.

(b) View 2.
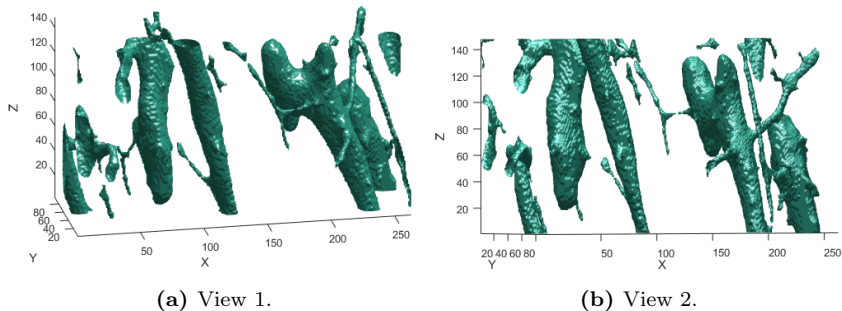
Figure 36: ISO surfaces of segmented canals in a sub-sample of the 1TS sample, from different views.

(a) View 1.

(b) View 2.

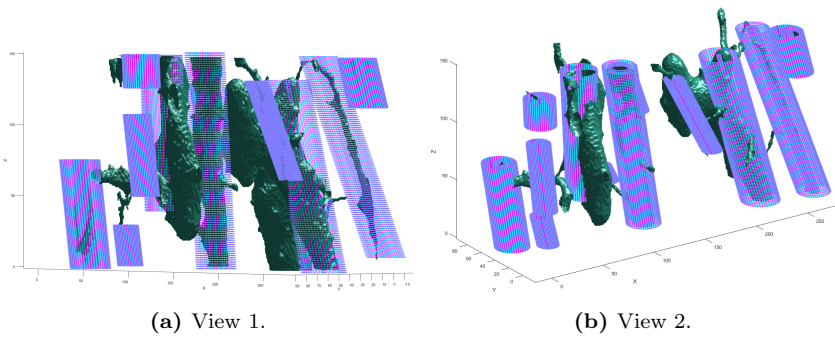**Figure 37:** ISO surfaces of segmented canals with cylinders fitted to Haversian canals and osteons, from different views.

(a) Transverse, xy-plane.
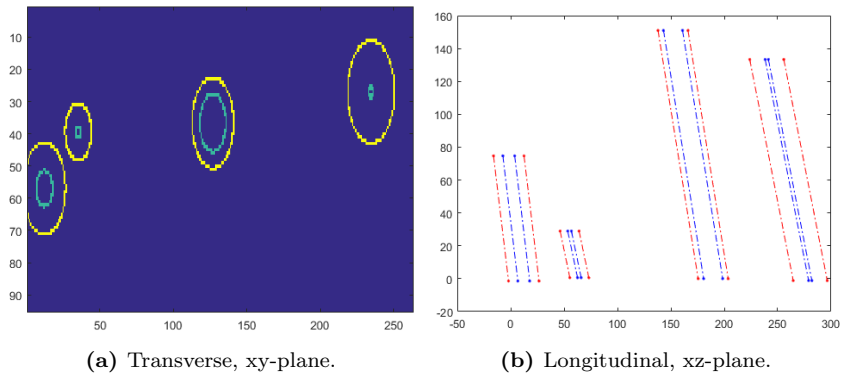
(b) Longitudinal, xz-plane.

Figure 38: 2D models, in different planes, based on the 3D model in Fig. 37.

56

8 Discussion

8.1 Segmentation

The segmentation method chosen (K-means clustering) sorts the pixels in the images into a number of different groups depending on intensity value. This makes the method sensitive to the intensity distribution in the images. If, e.g., the sample is not cortical but laminar, or if it contains no osteonal structures, the method will still label pixels with "osteonal intensities" as osteons leading to a faulty segmentation. This was most evident in the newly acquired sample images as the acquisition settings were slightly altered, leading to different intensity distributions compared to the images of the original ten samples. This also means that all types of structures with a specific pixel intensity will be grouped together, e.g. pores, non-Haversian canals, and Haversian canals. Hence, it is not possible to separate Haversian canals from the other types of structures which are of no interest for this project.

As is seen in Fig. 28 the segmentation of canals misses some structures, which are instead segmented as osteons. This is due to the variance in gray scale in the canals and osteons, where some canals are light enough to be clustered together with the osteons. This issue is not present in all samples, however, and can be mediated by changing the number of clusters used as canals to include one more, corresponding to the lighter gray pixels that are now wrongly segmented.

Fig 28 also shows how the osteonal segmentations were not optimal in terms of smoothness and separability. This issue arises due to two things:

1. The resolution of the μCT images makes it difficult to differentiate between different structures since, as stated before, more structures than the ones of interest have pixel intensities in the same interval as the ones used for segmentation.

2. The fact that the K-means algorithm does not take into consideration the spacial placement of data in relation to the cluster center, i.e. any pixel with intensity X will be grouped into cluster A, regardless of whether or not the pixel is close to a larger set of pixels with the same properties or if it is alone in a region with otherwise differing pixel intensities.

A better way of segmenting osteonal structures could be to use the K-means segmentation of the canals as seeds for growing regions until some threshold on how many pixels included in the region have intensities diverging from the intensity interval of osteonal structures. This could perhaps result in smoother osteonal segmentations with less noise, especially at higher image resolution. Another approach might be to look at the derivative, i.e. the change in pixel intensity over the border between osteon and interstitial bone. The derivative should be larger at this boarder than inside the osteon or in the interstitial bone, and hence it should be possible to find the osteonal edges.

Through trial and error it was determined that the optimal number of clusters was nine. This gave a good segmentation, based on the validation methods described in section 7.1.1 Validation, and kept the time and memory consumption manageable (see section 8.1.1 Runtimes). Having fewer clusters reduced the quality of the segmentations since the division of pixel intensities became more crude. The resulting segmentations hence had less detail. Having more clustered did enhance the detail in the segmentation but made segmenting larger image stacks extremely time consuming (>10 hours). Fig. 39 shows a comparison of different number of clusters applied to a sub-sample of the 1TS sample. For each different number of clusters, the canals, and osteons were created by using one third of the clusters, i.e. for three clusters canals, and osteons each got one cluster, for six clusters they each got two clusters, and for nine clusters they each got three clusters. The reduced quality of the segmentations is easiest seen when looking at the canal segmentations, where fewer structures are picked up the less clusters that are used.

(a) Canals, three clusters.

(b) Osteons, three clusters.

(c) Canals, six clusters.

(d) Osteons, six clusters.

(e) Canals, nine clusters.

(f) Osteons, nine clusters.
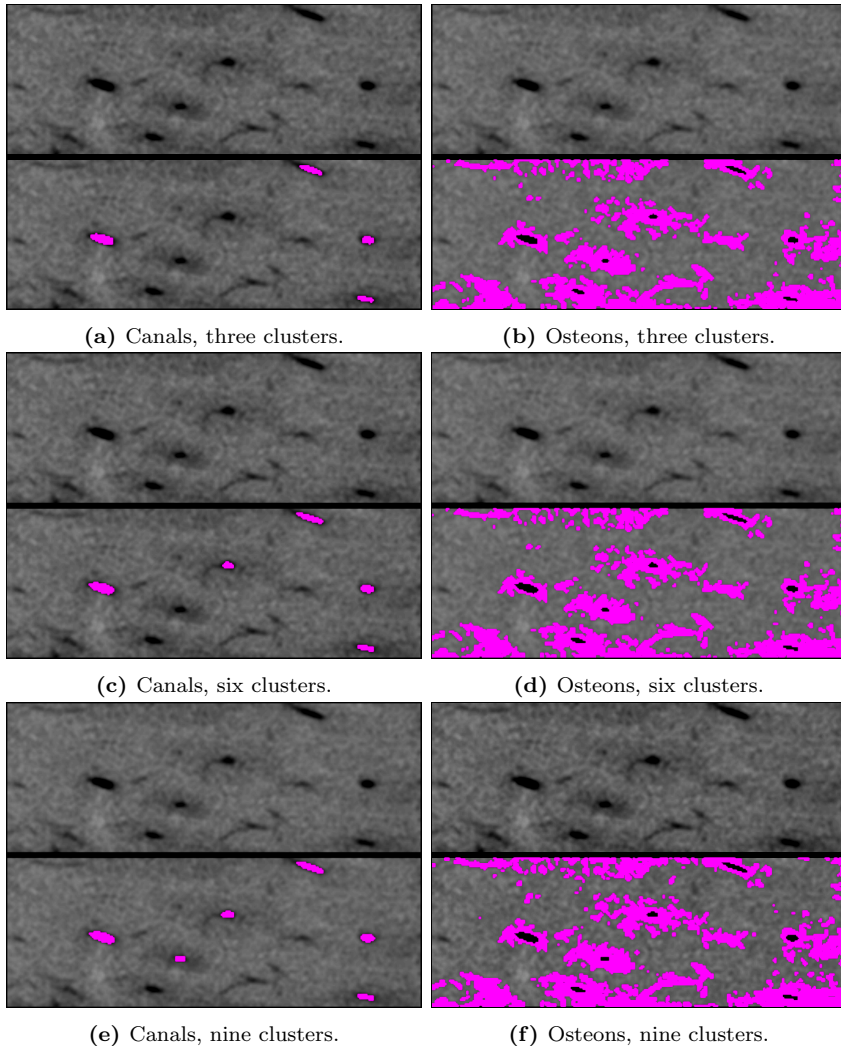
Figure 39: Segmentations, using different numbers of clusters, overlaid on top of their corresponding μCT image.

The K-means clustering was realized by putting all pixels, from all images in the image stack, into a 1D array. With larger image stacks this method was quite time consuming (see section 8.1.1 Runtimes) but resulted in a division of pixel intensities into clusters that was cohesive for all images. To enhance the speed of the K-means clustering, clustering each image on its own was tried. This reduced the runtime by 50-60% but caused the cluster labels to represent different pixel intensities in different images,

59

e.g. in image A cluster label X might correspond to the lowest intensity pixels, but in image B label X might correspond to some intermediate intensity. This was corrected for by indexing the labels with their corresponding image. However, not all replicates[12] of the clustering converged for all images which resulted in "missing" clusters in some images, i.e. in some images the pixels given label X and or Y were very few (less than 10) which meant that this label could not be used. Hence not all images contained a full set (nine) of labels resulting in a faulty division of labels into structures. An attempt to correct for this was made by skipping the missed labels but it was found that, due to the non-convergence of the clustering, the labels that were still present in the image had been given to pixels with intensities in different intervals than those in corresponding images. The resulting segmentation hence picked up the correct structures in some images but in other images the structures segmented corresponded to pixels originating in other structures, e.g. labels corresponding to canals in one image corresponded to osteons, or interstitial bone, in another image.

Using only six clusters for the background removal, instead of nine as in the final segmentation, was done in order to reduce time consumption. The resulting clustering proved to be efficient enough for identifying and removing background pixels. For two samples (see Fig. 11 and Fig. 40) the removal of background resulted in removal of parts of the sample as some of the canals and/or pores were extremely large and penetrated the sample, giving it the same characteristics as if a crack had been present, i.e. in images containing such large canals/pores the sample was divided into two or more segments depending on the geometry of the canal/pore. Fig. 41 shows the removal of background on such an image. This issue could be resolved by closing the edges of the sample before beginning the morphological operations; this would ensure that all internal structures are left after the removal of the background. However, this would cause the segmentation of samples containing cracks to be faulty as the edge closing would enclose the crack which would then be segmented together with canals and pores due to its similar pixel intensities. Since the issue with extremely large pores were only present in two out of the 27 samples segmented in this project, and since these samples were not representative of general cortical bone, it was decided not to implement the edge closing

---

[12]The clustering was repeated three times in order to reduce the risk of finding a local minimum instead of a global one (see section 5.3.1 Segmentation using K-means Clustering).

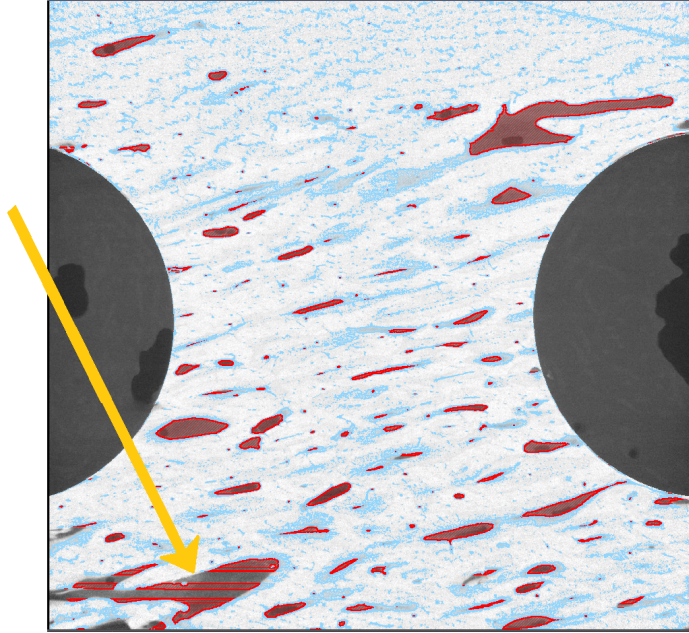fix but to make due with the less accurate segmentations of the two samples.

Figure 40: Sample 6TW overlaid with the segmented structures osteons (blue) and canals (red). The orange arrow points at a region in the sample where a canal is large enough to cause a faulty background removal, resulting in the loss of structures of interest in the segmentation.

(a) Original image.

(b) Labels used as background mask.

(c) Background mask after morphological operations for closing holes.

(d) Background mask after erosion and smoothing.

(e) Final image with background removed.
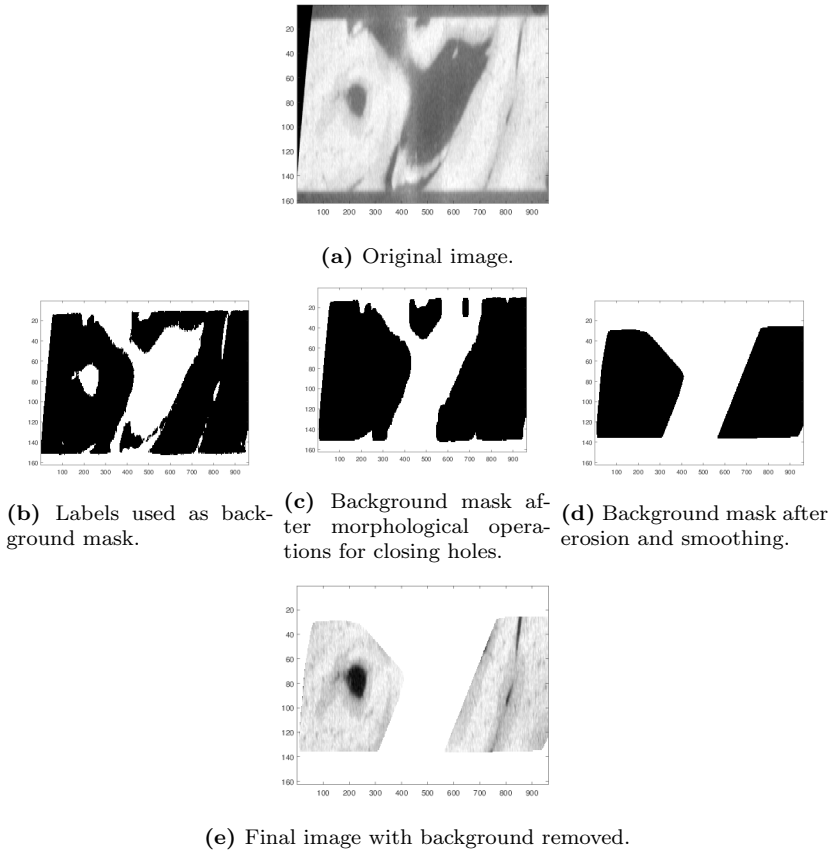
Figure 41: Evolution of background removal for a sample image with extremely large canals/pores. The final image has missing areas containing structures of interest and appears to contain a crack.

8.1.1 Runtimes

The runtime for the segmentation pipeline was measured for over 100 segmentations of image stacks corresponding to different samples and different subsamples. For each sample the time consumption was normalized against the file size in mega byte to enable comparison between the runs. The average runtime was 17 seconds per MB. The K-means clustering was the absolutely largest contributor to the time consumption.

The subsamples used for porosity analysis were about 7.25MB in size whilst the full sample files ranged between 700MB and 900MB, and the

high resolution samples between 700MB and 1550MB. Segmentation of a subsample hence took about 2 minutes, segmentation of a full samples between 3 hours 23 minutes and 4 hours 20 minutes, and segmentation of a high resolution sample took between 3 hours 23 minutes and 7 hours 28 minutes.

8.1.2   Validation

The K-means segmentations of canals fit well with the actual canals in the μCT images. However, some small structures are not picked up or are removed during the attempt at reducing noise by removing all structures with size below a certain threshold. This proves to be problematic as, on one hand, the segmentations become cleaner and easier to use, but on the other hand structures are removed and information lost. The segmentation of osteons is very un-smooth but covers areas that appear to be osteonal tissue. This issue is partially due to the fact that the K-means algorithm does not take into account the spatial distance of the pixels clustered together, which means that non-osteonal structures in the interstitial bone, with the same absorption properties as osteonal tissue and hence the same gray values in the μCT image, are segmented as osteons. The other reason for the un-smoothness is the incohesive gray levels inside the osteons, as is evident in Fig. 33d where osteonals regions are visible but contain gray levels that corresponds to interstitial bone based on the segmentation. Attempts to smooth the segmentation were made, but none gave good results.

One of the issues with manual segmentation is that it is very difficult to determine exact edges as well as keeping that decision constant in multiple samples. The implemented segmentation pipeline functions the same each time and hence comparison between samples is made easier and more accurate.

8.1.3   Sensitivity

Three main sources of sensitivity were found regarding the segmentation pipeline: The size of the file to be segmented, the pre-processing in terms of filtering, and the resolution of the images.

8.1.3.1 File size

Files over 600MB in size caused out of memory exception during the K-means clustering and could hence not be used as direct input to the pipeline. The fix was to divide such files into smaller parts and segmenting each part by its own before reassembling them by concatenation.

8.1.3.2 Filtering

Two different methods for filtering the μCT images were used: a Gaussian with a kernel of 0.8 followed by a mean filter with 1 pixel radius in ImageJ, or a Gaussian with a kernel of 0.8 in Matlab. Comparing each filtering method was tried separately, in both software; the differences between the filtering methods can be seen in Fig. 43. Comparing the mean pixel intensity in the Gauss filtered image (top right in Fig. 43) with the mean pixel intensity in the Gauss filtered image (top right in Fig. 42) and with the mean pixel intensity in the Gauss-mean filtered image (bottom right in Fig. 42) gives a difference of 0.0537 for both comparisons. However, when using K-means clustering for segmentation the resulting segmentation is very poor with the purely Gauss filtered images from ImageJ and the time consumption is much higher. Documentation for the plugin *Smooth (3D)* that was used for Gaussian filtering in ImageJ is non-existing and hence it is not possible to state what differs between this Gaussian filtering and the one used in Matlab.

Figure 42: Comparison between raw micro CT image (top left) and, in ImageJ, filtered micro CT image using only Gauss filter (top right), only mean filter (bottom left) and Gauss followed by mean filter (bottom right). The enhanced structure visibility between the raw image and the filtered images are obvious. This image is the first image from the sub-sample of the T1S sample (Fig. 10g).
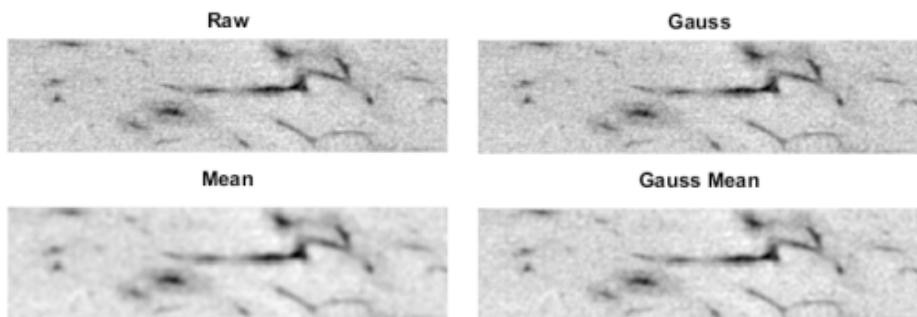
Figure 43: Comparison between raw micro CT image (top left) and, in Matlab, filtered micro CT image using only Gauss filter (top right), only mean filter (bottom left) and Gauss followed by mean filter (bottom right). The enhanced structure visibility between the raw image and the filtered images are obvious. This image is the first image from the sub-sample of the T1S sample (Fig. 10g).
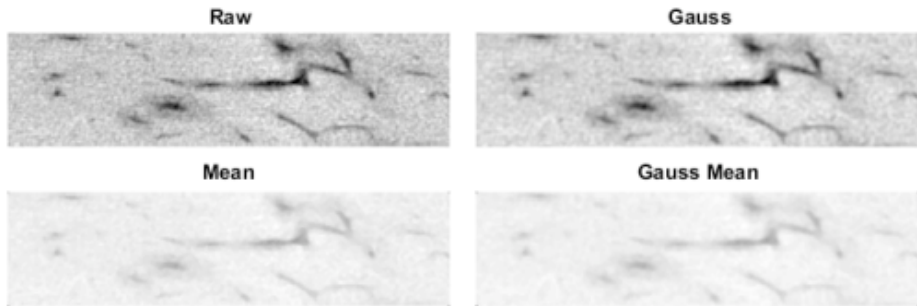
Fig. 44 shows a comparison between the resulting segmentations of a, in Matlab, filtered image stack and the same image stack with no filtering applied. It is clear that the un-filtered image results in a noisier segmentation, especially for the osteons, than the filtered image.

(a) Raw image. (b) Filtered image.
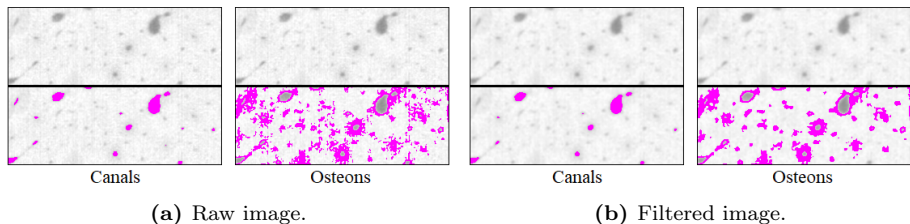
Figure 44: Comparison of segmentations of a μCT image in its raw state and after having been subjected to Gaussian filtering.

In Matlab larger kernel sizes (1.0, 1.3, 1.5, 1.8) were tried in order to see if a smoother segmentation could be achieved. The resulting segmentations were slightly smoother but due to the increased smoothing of the images some structures were missed in the segmentation and it was hence determined to stay with the kernel size of 0.8.

8.1.3.3 Image resolution

The most high resolution tomogram (voxels of 600nm) could not be used as it presented with artefacts, thought to be due to out of center rotation.

The other two higher resolution tomograms showed greatly enhanced visibility of the microstructure. The segmentation, however, was not enhanced as a result, as is seen in Fig. 32. Segmentation of canals was as good as before, but now small pores and canaliculi were also picked up. This was not completely problematic as a more correct porosity could be calculated based on these segmentations. However, since other microstructures than Haversian and non-Haversian canals were picked up the resulting segmentation was not immediately usable but had to have small structures, corresponding to the now distinguishable pores, removed. The segmentation of osteons was, however, worsened but the enhanced resolution as structures embedded in the interstitial bone, with similar mineralization as the osteons, were still picked up but were now more prominent. This led to the osteon segmentations being very noisy.

8.1.4   Structure Sizes and Porosity

As can be seen in Fig. 34a the calculated diameters of the Haversian canals does not correspond well with literature data, neither do the osteonal diameters which diverge a lot from the 150-200μm mentioned in literature. For one sample the mean diameter of the Haversian canals is even larger than the mean diameter of the osteons. This discrepancy is caused by the fact that the structures labels as osteons by the segmentation algorithm is not only actual osteons but also structures in the interstitial bone giving rise to pixels with the same intensity interval as osteons. The mean thickness of the osteons hence becomes less than expected as small non-osteonal structures affects the result. This issue might be alleviated by removing structures below some threshold size; this was tried but not optimized, as is obvious by the resulting segmentations. In Fig. 34b the expected difference between osteons and canals is seen. The large maximum diameters explains the large standard deviations seen for the mean thickness, as the microstructures in the sample have vastly different thickness, from very thin not-actual-structures-of-interest to very thick not-separated-structures. Again, the issue is separating structures of interest from pixels with similar intensities, and from each other. To properly analyse the diameters of both Haversian canals and osteons it is necessary to be able to look at the correct structure, not "noisy pixels", and to look at one structure at the time, not canals or osteons that are too close to be separable.

The porosity values for cortical bovine bone mentioned in the literature are 5-10% [Budyn et al., 2010, 2012; Manilay et al., 2013; Lee et al., 2012], which corresponds quite well to the values obtained here (see Tab. 5). Two have a higher porosity than what is shown but due to the excessive removal of background, as discussed in section 8.1 Segmentation, large regions corresponding to canals are missed by the segmentation pipeline, resulting in a lower-than-expected porosity. The majority of the plexiform samples (5L through 4TW Extra) have, as expected, lower porosities than the osteonal samples. The reason some osteonal samples display a lower porosity than expected from the literature is thought to be that too small canal structures are not being picked up by the segmentation algorithm.

8.2   Simplified Model

As can be seen in Fig. 26 the removal of branches resulted in the loss of some canal structures. This was due to the conditions used to determine what structures, in each of the three planes (xz, xy, yz), were to be removed. Due to these criteria some canals were incorrectly characterized as branches and hence removed. Changing the criteria slightly improved the result for some samples while worsening it for others, based on the shapes and sizes of the canals in the sample. A middle ground, where some information was lost but the resulting canal structures were still representative of the original sample, was in the end chosen for implementation.

As non-Haversian canals were removed from the model, the measured radii are more accurate and representative of the actual microstructure than the diameter values calculated for the segmentations (section 7.2 Simplified Model).

It was tried to identify branches based on intersection points, but this method requires that the "stem" can be identified and differentiated from the branches, based on a thickness difference between the "stem" and the branch, where the branch is thinner than the "stem", as well as that the branches are only connected to one "stem". Since the canal structures are extremely complex these conditions could not be met and the method was not usable.

Another method that was tried was converting the binary matrix of the canal structures into point clouds. This enables identification of orienta-

tion for each point in the cloud. The idea was that it might be possible to identify points corresponding to branches by looking at the orientation of the points. This turned out not to work because of the non-smooth nature of the structures, which caused points in branches, and in "stems", to not have a homogeneous orientation, and hence it was not possible to separate branch-points from "stem"-points.

A different approach to the implementation of the simplified model might be to determine the porosity of the sample, as well as a set of average radii for both Haversian canals and osteons. The model could then be created by choosing radii randomly from the set, and putting as many structures into a volume as needed to fit the porosity measurement. However, the issue regarding what structures are used to measure porosity remain. If it is possible to only look at Haversian canals, the porosity value will be true, but this has proven difficult. Also, this approach would not capture the tilts of the structures.

The biggest issue, however, is that it is not possible to validate the model by other means than comparing calculated radii to thickness calculations for the corresponding segmentations, and by visually comparing the cylinders, in terms of origin and end, tilt and radii, to the ISO surfaces of the canals in the generated plot. As the microstructure is so complex, it is not easy to generalize and simplify it.

9 Conclusion and Future Work

A semi-automatic method for segmentation and modelling of Haversian canals and osteons has been developed in accordance with the aims of the project.

K-means clusterings can be used to successfully segment Haversian canals, and osteons from μCT images at different levels of resolution. The segmented canals give porosity values that correspond well with literature. However, the method is not optimal for the segmentation of osteonal structures, especially at resolutions below $\sim 9\mu$m, as structures with similar densities in the interstitial bone result in the same pixel intensities as the osteonal structures and hence are segmented out together with the osteonal structures. While this is a problem already at 9μm voxel size, giving rise to noisy and un-smooth osteonal segmentations, the issue worsens at higher resolution. Hence, the geometry of the segmented osteons corresponds badly with the geometry of the actual osteonal structures in the samples. The method needs to be improved, in terms of smoothness of the segmentations, for it to give good results in terms of geometry and volume.

In the implementation of the simplified model, non-Haversian canals are identified and removed by looking at whether or not they are surrounded by osteonal structure. Identifying Haversian canals this way also in the segmentation pipeline could improve the accuracy of the segmentation.

After minor further improvements, in terms of size thresholds and output segmentations, it will be possible to use the pipeline to segment canaliculi structures, separate from canals, in higher resolution images. Also, changing the cluster division and number of segments, would enable the segmentation pipeline to be used for segmenting canals and pores in non-osteonal cortical bone. This would be useful in terms of porosity analysis of samples.

Modelling the cortical microstructure by fitting cylinders results in a good representation of the structures in terms of radii, placement, and tilt. However, the fitting of cylinders to the segmented microstructures is not optimal. Some structures are missed by the pipeline due to difficulty in removing branched canals, and hence a great opportunity for improvement would be to optimize the branch removal. It might be possible to combine the method of finding intersection points with manual input, in

that the user tells the software what is "stem" by e.g. clicking on points in a plot. The algorithm then needs to be altered so that it is not size dependent and so that it can handle branches connected to multiple "stems". Another possibility could be to let the user mark out top and bottom of a canal and only look at points inside some length interval when evaluating that canal. That way branches would not interfere with the tilt, and radii analysis. However, this might be difficult to implement as many samples are very cluttered in terms of clusters of branched canals.

References

S. Li, A. Abdel-Wahab, E. Demirci, and V. V. Silberschmidt. Fracture process in cortical bone: X-fem analysis of microstructued models. *International Journal of Fracture*, 184:43–55, 2013.

S. Mischinski and A. Ural. Interaction of microstructure and microcrack growth in cortical bone: A finite element study. *Computer Methods in Biomechanics and Biomedical Engineering*, 5842:1–14, 2011.

A. Demirtas, E. Curran, and A. Ural. Assessment of the effect of reduced compositional heterogeneity on fracture resistance of human cortical bone using finite element modeling. *Bone*, 91:92–101, 2016.

Neashan Mathavan. Loading/dic/saxs measurements of bone. PDF. Instructions.

F. H. Martini. Fundamentals of anatomy and physiology, 9:th edition - chapter 6: Osseous tissue and bone structure. PowerPoint Lecture Presentation, by Jason LaPres, 2012. URL `https://learning.hccs.edu/faculty/alicia.cummings/biol2401/powerpoint-slides/chapter-6-pdf-slides`. Visited on: 2017-04-25.

OpenStax College. File:603 anatomy of long bone.jpg, 2013. URL `https://commons.wikimedia.org/wiki/File:603_Anatomy_of_Long_Bone.jpg`. Visited on: 2017-05-05.

A. G. Robling and S. S. Stout. *Biological Anthropology of the Human Skeleton, Chapter 5 - Histomorphometry of Human Cortical Bone: Applications to Age Estimation.* John Wiley & Sons, Inc., Hoboken, New Jersey, 2008.

É. Budyn, J. Jonvaux, C. Funfschilling, and T. Hoc. Bovine cortical bone stiffness and local strain are affected by mineralization and morphology. *Journal of Applied Mechanics*, 79(1), 2010.

É. Budyn, J. Jonvaux, and T. Hoc. Bio-morphing of progressive pathologies in haversian cortical bone. *Journal of Applied Mechanics*, 79(2), 2012.

I. S. Maggiano, C. M. Maggiano, J. G. Clement, C. D. L. Thomas, Y. Carter, and D. M. L. Cooper. Three-dimensional reconstruction of haversian systems in human cortical bone using synchrotron radiation-based micro-ct: Morphology and quantification of branching and traverse connections across ages. *Journal of Anatomy*, 228:719–732, 2016.

R. O. Ritchie. How does human bone resist fracture? *Annals of The New York Academy of Sciences*, 1192:72–80, 2010.

M. Langer and F. Peyrin. 3d x-ray ultra-microscopy of bone tissue. *Osteoporosis International*, 27:441–455, 2016.

R. O. Ritchie, J. H. Kinney, J. J. Kruzic, and R. K. Nalla. A fracture mechanics and mechanistic approach to the failure of cortical bone. *Fatigue & Fracture of Engineering Materials & Structures*, 28(4):345—-371, 2005.

K. J. Koester, J. W. Ager, and R. O. Richie. The true toughness of human cortical bone measured with realistically short cracks. *Nature Materials*, pages 672–677, 2008.

Wikimedia Commons. Murhocorticalbone.jpg, 2001. URL `https://commons.wikimedia.org/wiki/File:MurhoCorticalBone.jpg`. Visited on: 2017-03-24.

J. T. Bushberg, J. A. Seibert, E. M. Jr. Leidholdt, and J. M. Boone. *The Essential Physicts of Medical Imaging*. Lippincott Williams and Wilkins, Philadelphia, 3rd edition edition, 2012.

J. Hsieh. *Computed tomography: Principles, Design, Artifacts, and Recent Advances*. SPIE Press, Bellingham, 2nd edition edition, 2009.

E. N. Landis and D. T. Keane. X-ray microtomography. *Materials Characterization*, 61(12):1305–1316, 2010.

R. Mizutani and Y. Suzuki. X-ray microtomography in biology. *Micron*, 43:1014–115, 2012.

F. E. Boas and D. Fleischmann. Ct artifacts: Causes and reduction techniques. *Imaging in Medicine*, 4(2):229–240, 2012.

T. Hägglund. Reglerteknik ak - föreläsningar. Compendium, 2012. Chapter 13.4 - Sampling.

C. M. Bishop. *Pattern Recognition and Machine Learning.* Springer Science, 233 Spring Street New York NY 10013 USA, 2009.

R. Szeliski. *Computer Vision: Algorithms and Applications.* Springer-Verlag, London, 2011. Chapter 5: Segmentation.

S. P. Lloyd. Least squares quantization in pcm. *IEEE Transactions on Information Theory*, 28:129–137, 1982.

LTH Solid Mechanics, Faculty of Engineering. 4d imaging lab. URL `http://www.solid.lth.se/resources/4d-imaging-lab/`. Visited on: 2017-01-10.

J. Schindelin, I. Arganda-Carreras, and E. Frise et al. Fiji: An open-source platform for biological-image analysis. *Nature methods*, 9(7): 676–682, 2012.

C. A. Schneider, W. S. Rasband, and K. W. Elicieri. Nih image to imagej: 25 years of image analysis. *Nature methods*, 9(7):671–675, 2012.

CIBC, 2016. Seg3D: Volumetric Image Segmentation and Visualization. Scientific Computing and Imaging Institute (SCI), Download from: http://www.seg3d.org.

T. Ferreira and W. Rasband. Imagej user guide, 2012. URL `https://imagej.nih.gov/ij/docs/guide/146-29.html`. Visited on: 2016-12-06.

MathWorks. convhull, 2017. URL `https://se.mathworks.com/help/matlab/ref/convhull.html`. Visited on: 2017-04-25.

M. de Berg, O. Cheong, M. van Kreveld, and M. Overmars. *Computational Geometry - Algorithms and Applications.* Springer-Verlag, Berlin, Heidelberg, 3:rd edition edition, 2008. Chapter 1: Computational Geometry - Introduction.

MathWorks. kmeans, 2016a. URL `https://se.mathworks.com/help/stats/kmeans.html`. Visited on: 2017-02-10.

MathWorks. pca, 2016b. URL `https://se.mathworks.com/help/stats/pca.html`. Visited on: 2017-02-16.

Richard Brown. fitcircle.m, 2007. URL `https://se.mathworks.com/matlabcentral/fileexchange/15060-fitcircle-m`. Visited on: 2017-02-16.
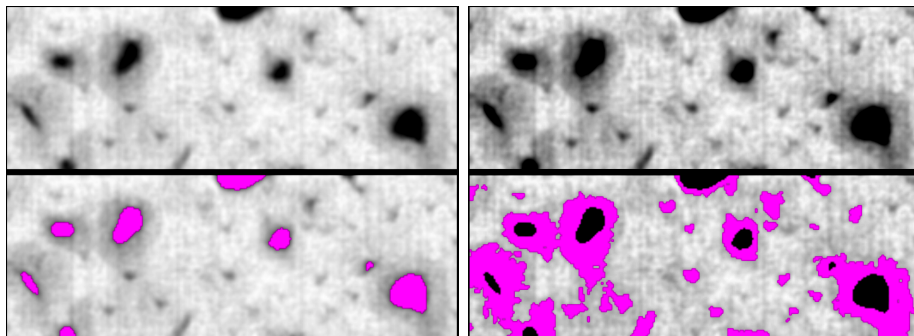
MathWorks. imfill.m, 2006. URL `https://se.mathworks.com/help/images/ref/imfill.html`. Visited on: 2017-02-16.

M. Doubeand, M. M. Klosowski, and I. Arganda-Carreras et al. Bonej: Free and extensible bone image analysis in imagej. *Bone*, 47(6):1076–1079, 2010.

A. Mayya, A. Banerjee, and R. Rajesh. Haversian microstructure in bovine femoral cortices: An adaptation for improved compressive strength. *Materials Science and Engineering: C*, 59:454–463, 2016.

W. Zhang, S. A. Tekalur, and Z. Zhong. Microcracking morphology and structure optimization of compact bovine bone under impact loading. *Conference Proceedings of the Society for Experimental Mechanics Series*, 4:123–126, 2014.

D. Carnelli, P. Vena, M. Dao, C. Ortiz, and R. Contro. Orientation and size-dependent mechanical modulation within individual secondary osteons in cortical bone tissue. *Journal of the Royal Society*, 10:72–80, 2013.

Z. Manilay, E. Novitskaya, E. Sadovnikov, and J. McKittrick. A comparative study of young and mature bovine cortical bone. *Acta Biomaterialia*, 9(2):5280–5288, 2013.

S. Lee, M. Porter, S. Wasko, G. Lau, P. Chen, E. E. Novitskaya, A. P. Tomsa, A. Almutairi, and M. A. Meyers an J. McKittrick. Potential bone replacement materials prepared by two methods. *MRS Proceedings*, 1418, 2012.

A   Sample ID's and Dimensions

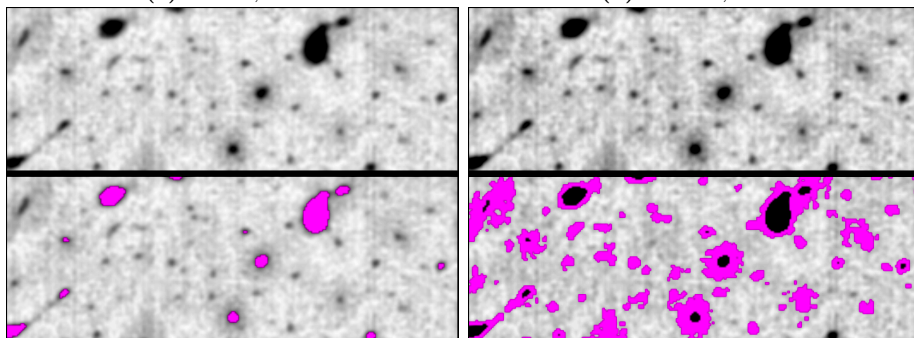**Table 6:** Sample ID, dimensions, and thickness, for the samples used in the main project.

ID	Dimensions	Thickness
P1	-	-
P2	-	-
1L	40×20 mm	~ 1 mm
1LW	40×20 mm	1 mm
1LW Extra	40×20 mm	1 mm
2LW	30×20 mm	~ 1 mm
2LS	30×20 mm	1 mm
2LS Extra	40×20 mm	1 mm
3L	40×20 mm	1.1 mm
3LW	40×20 mm	1 mm
3LW Extra	40×20 mm	1.0 mm
3LS	40×20 mm	1.0 mm
4L	40×20 mm	0.85 mm
4LW	40×20 mm	1 mm
4LS	40×20 mm	~ 1 mm
5L	40×20 mm	1.15 mm
5LS	40×20 mm	0.7 mm
1TW	30×20 mm	1.2 mm
1TS	30×20 mm	1.2 mm
2TS	30×20 mm	1 mm
4TW	30×20 mm	1.3 mm
4TW Extra	40×20 mm	1 mm
4TS	30×20 mm	1.3 mm
5TS	30×20 mm	1 mm
6T	30×20 mm	1.2 mm
6TW	30×20 mm	1.3 mm
6TS	30×20 mm	1.3 mm

B Segmentation of Cortical Bone - Overlays

(a) Canals, 2LW.

(b) Osteons, 2LW.

(c) Canals, 2LS.

(d) Osteons, 2SL.
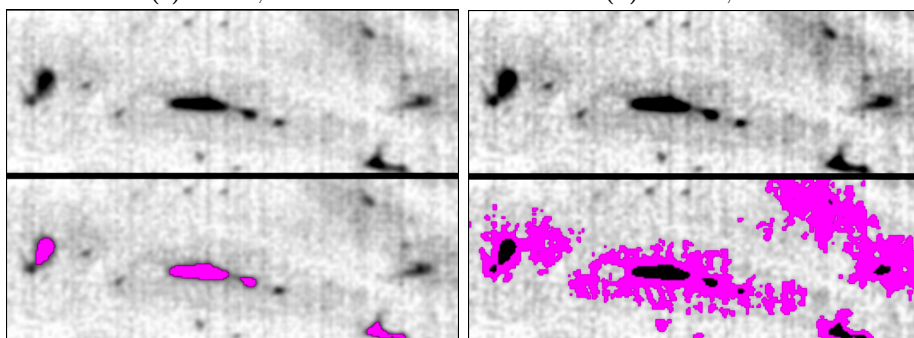
(e) Canals, 1TW.

(f) Osteons, 1TW.
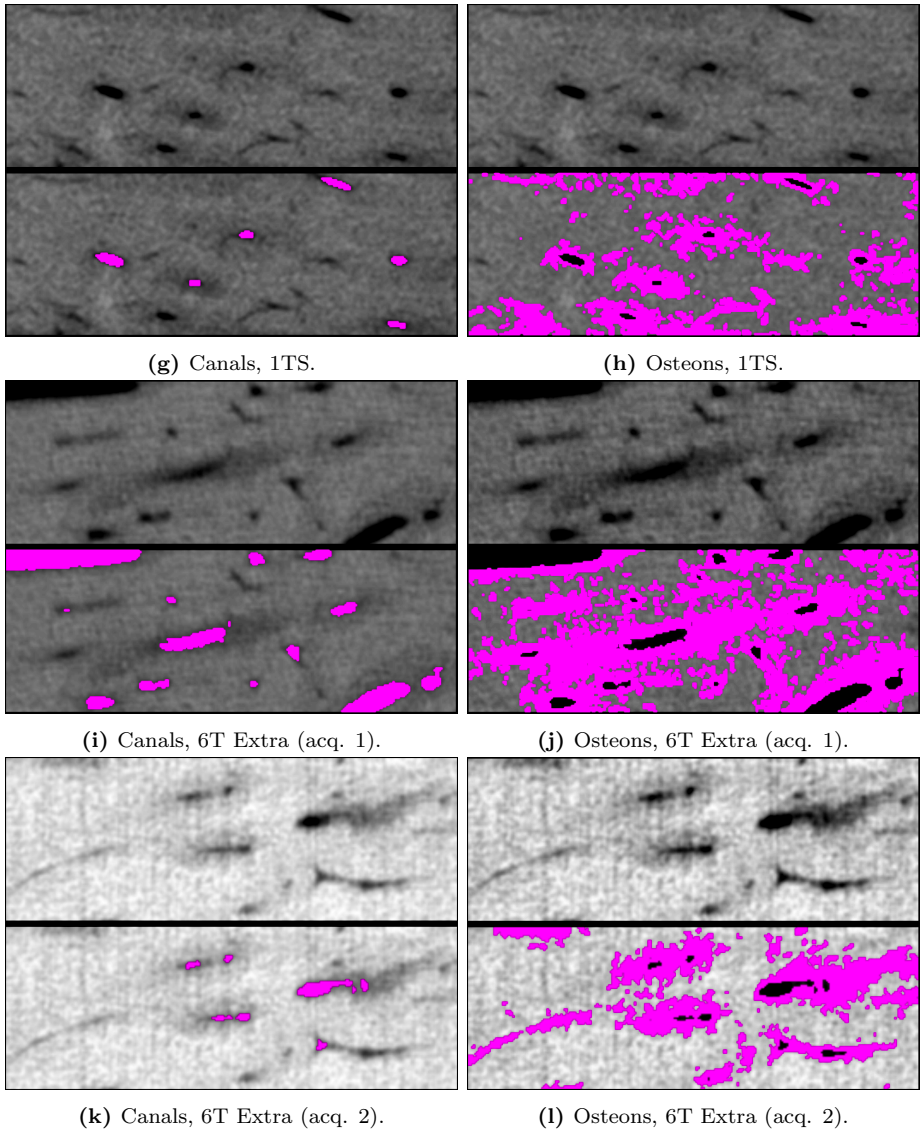
(g) Canals, 1TS.

(h) Osteons, 1TS.

(i) Canals, 6T Extra (acq. 1).

(j) Osteons, 6T Extra (acq. 1).

(k) Canals, 6T Extra (acq. 2).

(l) Osteons, 6T Extra (acq. 2).

Figure 45: Segmentations of sub-samples from the six osteonal bone samples. The segmentation has been overlaid (magenta) on top of the original μCT image. Fig. 45g, 45h, 45k, and 45l differ in gray scale from the other samples due to them being imaged during the first tomograph session.